# A global analysis of the asymmetric effect of ENSO on extreme precipitation

X. Sun, Benjamin Renard, M. Thyer, S. Westra, M. Lang

# A global analysis of the asymmetric effect of ENSO on extreme precipitation

Xun SUN[1], Benjamin RENARD[2], Mark THYER[3], Seth WESTRA[3], Michel LANG[2]

Correspondence to: Dr. X. Sun.

E-mail address: xs2226@columbia.edu

[1] Columbia Water Center, Columbia University, New York, NY 10027, USA

[2] Irstea, UR HHLY, centre de Lyon-Villeurbanne, F-69626 Villeurbanne, France

[3] School of Civil, Environmental & Mining Engineering, University of Adelaide, SA, 5005, Australia

*Abstract*

The global and regional influence of the El Niño-Southern Oscillation (ENSO) phenomenon on extreme precipitation was analyzed using a global database comprising over 7000 high quality observation sites. To better quantify possible changes in relatively rare design-relevant precipitation quantiles (e.g. the 1 in 10 year event), a Bayesian regional extreme value model was used, which employed the Southern Oscillation Index (SOI) – a measure of ENSO – as a covariate. Regions found to be influenced by ENSO include parts of North and South America, southern and eastern Asia, South Africa, Australia and Europe. The season experiencing the greatest ENSO effect varies regionally, but in most of the ENSO-affected regions the strongest effect happens in boreal winter, during which time the 10-year precipitation for |SOI|=20 (corresponding to either a strong El Niño or La Niña episode) can be up to 50% higher or lower than for SOI=0 (a neutral phase). Importantly, the effect of ENSO on extreme precipitation is asymmetric, with most parts of the world experiencing a significant effect only for a single ENSO phase. This finding has important implications on the current understanding of how ENSO influences extreme precipitation, and will enable a more rigorous theoretical foundation for providing quantitative extreme precipitation intensity predictions at seasonal timescales. We anticipate that incorporating asymmetric impacts of ENSO on extreme precipitation will help lead to better-informed climate-adaptive design of flood-sensitive infrastructure.

**Keywords**: ENSO, asymmetric relationship, extreme precipitation, Bayesian regional modeling, GEV distribution, climate-informed model

# 1 INTRODUCTION

Every year, extreme precipitation results in flooding that leads to loss of life and infrastructure, as well as economic disruption. Not only are the direct effects of floods felt for many years, but the indirect effects - including disease, trauma and social dislocation, reduced agricultural production or loss of manufacturing capacity - can be felt for decades (Ahern et al., 2005). The El Niño-Southern Oscillation (ENSO) is the single most influential climate phenomenon affecting the variability of global precipitation extremes (Dai et al., 1997), and understanding the ENSO-extreme precipitation relationship is therefore critical to predict and manage the impacts of floods at global and regional scales (Ward et al., 2014a; Ward et al., 2014b). While many previous studies have detected the ENSO impact on extreme precipitation indices, this study is the first to undertake a global analysis that quantifies the asymmetric impact of ENSO on "design-relevant" extreme precipitation quantiles (e.g. the 1 in 10 year event).

A large number of studies have discussed the relationship between the two ENSO phases (El Niño and La Niña) and regional average precipitation. Ropelewski and Halpert (1987) provided a global pattern of the magnitude, phase and duration of ENSO-related precipitation. Dai et al. (1997) and Dai and Wigley (2000) also examined precipitation over the oceans and described a global pattern of the effect of ENSO on precipitation. In boreal winter, positive anomalies occur in southwestern North America during El Niño episodes and northwestern North America during La Niña episodes (Castello and Shelton, 2004; Meehl et al., 2007). Positive anomalies occur during El Niño episodes in southeastern South America in austral winter, spring and summer, and northeastern South America in autumn (Fernandez and Fernandez, 2002; Grimm, 2011; Kayano and Andreoli, 2006). La Niña enhances the rainfall in South Africa in summer (Kruger, 1999; Vanheerden et al., 1988),

and significant effects are also found in Asia (Kane, 1999; Kripalani and Kulkarni, 1997; Li and Ma, 2012; Wu et al., 2003) and Australia (Cai and Cowan, 2009).

Although many of the early studies of the ENSO-precipitation relationship focus on seasonal and annual average precipitation, an increasing number of studies have begun to focus on the relationship between ENSO and extreme precipitation, given its importance in understanding flood risk. For instance, a significant ENSO influence was found on the frequency of extreme precipitation in North America (Cayan et al., 1999; Gershunov and Barnett, 1998; Higgins et al., 2011; Jones and Carvalho, 2012; Schubert et al., 2008) and South America (Grimm and Tedeschi, 2009; Pscheidt and Grimm, 2009). This relationship had also been studied in China (Wan et al., 2013) and Australia (Min et al., 2013). At the global scale, Curtis et al. (2007) investigated the correlation between ENSO and the frequency of estimated precipitation extremes for different seasons, while Lyon and Barnston (2005) discussed the spatial extent of tropical land precipitation extremes related to the extreme phases of ENSO. Kenyon and Hegerl (2010) reported on the response of global extreme precipitation to ENSO. Alexander et al. (2009) studied the global response of precipitation extremes to global sea surface temperature variability.

A limitation of many of these studies is that the "extremes" investigated are still relatively frequent events, and thus not directly meaningful from a flood risk estimation perspective. For example, Cayan et al. (1999) used the daily precipitation larger than the $90^{th}$ percentiles (P90), while Lyon and Barnston (2005) used an index based on monthly precipitation anomalies from a gridded dataset. In contrast, the design, management and operation of water-related engineering infrastructure often requires information on rarer "design-relevant" extremes, such as the 1 in 10 year or 1 in 100 year precipitation event (Westra et al., 2014). The rarity of such events makes detecting an association between extreme rainfall and ENSO difficult, and a framework for

quantifying such effects is therefore required to assist with the design and operation of engineering systems that can adapt to ENSO-induced climate variability.

To move beyond simply detecting the ENSO effect on extreme precipitation indices and instead focus on estimating ENSO effect on extreme precipitation quantiles that are "design-relevant", one needs to account for the specific features of extreme precipitation. Challenges with estimating extreme precipitation quantiles include:

1. At-site extremes are much more variable than temporally or spatially averaged precipitation. As a consequence, detecting an ENSO effect is more difficult due to a lower signal-to-noise ratio, which raises questions on the ability of local methods to detect ENSO effects;
2. Extreme precipitation usually occurs over a small spatial area within a short time. Thus, spatially smoothed datasets, such as gridded datasets, are not well-adapted. As an illustration, Mannshardt-Shamseldin et al. (2010) showed that raingauge-based precipitation quantiles may be two to three times higher than gridded precipitation quantiles. However, the use of raingauge-based data poses specific difficulties in terms of irregular spatial sampling and handling of missing data; and
3. Quantifying ENSO effects on extreme precipitation requires use of appropriate probabilistic models (i.e. extreme value distributions).

To analyze and predict the impact of climate variability on extreme hydrological variables, several non-stationary and climate-informed frequency analysis (FA) models have been developed at both local scale (e.g. Renard et al. (2006b), Kwon et al. (2008), Ouarda and El-Adlouni (2011), Tramblay et al. (2012)) and regional scale (e.g. Renard et al. (2006a), Hanel et al. (2009), Aryal et al. (2009), Lima and Lall (2010b), Shang et al. (2011), Westra and Sisson (2011)). Local analyses generally lead to large uncertainties that may mask the ENSO effect. Although regional analyses

may improve the detection power, additional difficulties are induced by the inherent spatial structure of precipitation. Furthermore, most of the aforementioned regional studies ignore spatial dependence (an exception being Westra and Sisson (2011)).

Another limitation of many previous studies that describe the ENSO-precipitation teleconnection is that they often assumed a symmetric relation (with anomalies during El Niño being the opposite of those during La Niña (Hoerling et al., 1997)), however this assumption is increasingly being questioned. Several studies have demonstrated asymmetric associations between ENSO and climate variables (e.g., pressure and precipitation) (Hannachi, 2001; Hoerling et al., 2001; Hoerling et al., 1997; OrtizBevia et al., 2010; Sardeshmukh et al., 2000). Asymmetry has been reported for the ENSO effect on regional rainfall for the winter precipitation response in North America by Wu et al. (2005), and for the spring rainfall in south China and Taiwan by Feng and Li (2011) and Chen et al. (2008). In Australia, the asymmetric effect of ENSO on extreme precipitation has been described for southeast Queensland (Cai and van Rensch, 2012; Cai et al., 2010; Sun et al., 2014) and eastern Australian regions (King et al., 2013). Importantly, Sun et al. (2014) showed that, compared to the asymmetric ENSO-precipitation model, the assumption of either no ENSO effect or only a symmetric ENSO-precipitation relationship led to a strong underestimation of extreme precipitation quantiles in southeast Queensland during La Nina episodes. This has significant practical implications for the design and management of flood-sensitive engineering infrastructure. Hence, there is a clear need to develop a global perspective on the form of the extreme ENSO-precipitation relationship, in particular for extreme precipitation quantiles.

This study provides the first quantitative assessment of the global asymmetric effect of ENSO on seasonal “design-relevant” extreme daily precipitation. We extend the study of Sun et al. (2014) to a new global high quality gauge-based observation dataset (HadEX2) comprising observations at over

7000 stations (Donat et al., 2013). The same climate-informed Bayesian regional frequency analysis (RFA) method that was developed in Sun et al (2014) is applied to analyze the at-site extremes across this larger spatial domain. This method enables detecting and quantifying the effect of climate variability on extreme precipitation with the consideration of spatial dependence, and can account for situations where records at each site are of different lengths and contain missing values. Furthermore, the fact that ENSO effects are regionalized yields more precise estimates of the ENSO-extreme precipitation relationship compared to at-site analysis, while also providing sufficient resolution to identify distinct regional features. We apply this regional frequency analysis approach to geographic regions covering all land areas. The contribution is highlighted from the perspective of engineering design, which requires considering at-site extremes, rather than spatially smoothed gridded data sets. This makes the key difference with other studies that analyzed the relationship between ENSO and extreme precipitation at a large scale.

This paper is organized as follows. Section 2 presents the dataset and briefly outlines the climate-informed RFA framework applied to extreme precipitation. Section 3 assesses several assumptions made by the RFA model and justifies its application on the global data set. Section 4 describes the main results of the analysis, including the ENSO effect on extreme precipitation and the possible asymmetry of this effect. Practical implications and further improvements are discussed in Section 5. Section 6 summarizes the main findings of the study.

## 2 DATA AND METHOD

### 2.1 Data

The Hadley Center Global Climate Extremes Index 2 (HadEX2) dataset (Donat et al., 2013) comprises the monthly maxima of daily precipitation from 11,588 high quality observation sites

(Figure 1). The 7037 sites with records longer than 40 years were used, with a median record length of 60 years. The highest density of gauges is in Europe, the United States and South Africa, and the lowest density is in Amazonia, most of Africa, central Asia, tropical areas of Asia and central Australia. Overall, temperate climate areas are much more represented than tropical or subtropical ones, while polar areas are very scarcely gauged. For each site, we calculated the seasonal maxima of daily precipitation for December-January-February (DJF), March-April-May (MAM), June-July-August (JJA) and September-October-November (SON).

The Southern Oscillation Index (SOI) is a measure of the strength of ENSO. The index is calculated from the monthly mean sea level pressure difference between Tahiti and Darwin. Typically, as presented in the website of Australian Bureau of Meteorology (BOM) (http://www.bom.gov.au/climate/glossary/soi.shtml), sustained negative SOI values below about –8 indicate an El Niño event while sustained positive values above +8 indicate a La Niña event, although for simplicity we refer to a negative value of the SOI as an El Niño and a positive value as a La Niña. The SOI data (1877-2011) used in this study were obtained from the BOM website, and were seasonally averaged using the same seasons as for precipitation.

### 2.2 A regional extreme value model

We apply a climate-informed regional frequency analysis (RFA) method to evaluate the effect of ENSO on extreme precipitation. This framework includes: (1) A generalised extreme value (GEV) model for extreme precipitation; (2) GEV parameters dependent on covariates based on indices of ENSO (SOI); (3) Spatial dependence represented by a Gaussian copula; (4) Bayesian inference techniques to provide reliable estimates of parameter and predictive uncertainty. Reliable estimates of parameter uncertainty are essential for models of extremes precipitation because the data lengths are short and the parameter uncertainty is a significant component of the predictive uncertainty.

A complete presentation of the method along with comparisons of alternative model formulations is given by Sun et al. (2014), and the methodology is summarized briefly here.

### 2.2.1 Probabilistic regional model

The generalized extreme value (GEV) distribution (Fisher and Tippett, 1928) is often used to describe the distribution of annual or seasonal maxima. The cumulative distribution function (cdf) of the GEV distribution is:

$$G(y \mid \mu, \sigma, \xi) = \exp\left( -\left[ 1 - \xi\left( \frac{y-\mu}{\sigma} \right) \right]^{1/\xi} \right) \quad (1)$$

where $\mu$, $\sigma$ and $\xi$ are the location, scale and shape parameters, respectively. In the following, we call these three parameters the D-parameters (i.e., distribution parameters).

For a given region, the observed seasonal maximum at site $s$ and time $t$ is a realization from the random variable $Y(s,t)$. To develop the regional model, a GEV distribution is assumed for all sites (Coles et al., 2003; Katz et al., 2002) with D-parameters allowed to vary in both space and time:

$$Y(s,t) \sim GEV(\mu(s,t), \sigma(s,t), \xi(s,t)) \quad (2)$$

For each D-parameter, a regression function is used to link the parameter value with the temporally-varying covariate SOI. Following Sun et al. (2014), a piecewise linear regression function for the location and scale parameters is used to separately evaluate the effect of ENSO during the El Niño and La Niña phases. We do not assume any ENSO-related regression functions for the shape parameter since this parameter is difficult to estimate even in a stationary context (Coles, 2001, p106).

Because ENSO is a large-scale (global) mode of variability, we reason that the influence of ENSO on precipitation would be a slowly varying function in space, and have therefore assumed that some

196 regression parameters would be constant for all sites within a geographic region (defined in Section
197 2.2.2). This regional approach results in reduced uncertainty of parameters and predictions relative
198 to estimating parameters separately at each gauge, as had been demonstrated in a number of
199 previous studies (e.g., Renard et al. (2006a); Hanel et al. (2009); Westra and Sisson (2011); Sun et
200 al. (2014)).
201
202 The regression function for each D-parameter is therefore given by:

203
$$\mu(s,t) = \begin{cases} \mu_{loc_0}^{(s)} + \mu_{reg_1}^{-} * SOI(t); SOI(t) < 0, \text{El Niño} \\ \mu_{loc_0}^{(s)} + \mu_{reg_1}^{+} * SOI(t); SOI(t) > 0, \text{La Niña} \end{cases} \quad (3a)$$

204
$$\sigma(s,t) = \begin{cases} \sigma_{loc_0}^{(s)} + \sigma_{reg_1}^{-} * SOI(t); SOI(t) < 0, \text{El Niño} \\ \sigma_{loc_0}^{(s)} + \sigma_{reg_1}^{+} * SOI(t); SOI(t) > 0, \text{La Niña} \end{cases} \quad (3b)$$

205
$$\xi(s,t) = \xi_{reg} \quad (3c)$$

206 We denote $\theta_{loc}^{(s)} = (\mu_{loc_0}^{(s)}, \sigma_{loc_0}^{(s)})$ and $\theta_{reg} = (\mu_{reg_1}^{-}, \mu_{reg_1}^{+}, \sigma_{reg_1}^{-}, \sigma_{reg_1}^{+}, \xi_{reg})$ as regression parameters that
207 need to be estimated. $\theta_{loc}^{(s)}$ are site-specific (local) parameters, while $\theta_{reg}$ are regional parameters
208 which are common for all sites within the region. The use of piecewise linear regression functions
209 outlined in Eq. (3), with different linear functions in the El Niño and La Niña phases, enables the
210 modelling framework to capture and evaluate the asymmetric nature of the ENSO-precipitation
211 relationship.
212
213 Spatial dependence between data inside a region is described with a Gaussian copula as used in Sun
214 et al. (2014). The dependence matrix $\Sigma$ for the Gaussian copula is:

215
$$\Sigma(s_i, s_j) = \eta_1 \exp(-\eta_2 * \| s_i, s_j \|) \quad (4)$$

216 where $\| s_i, s_j \|$ is the distance between sites $s_i$ and $s_j$, and $\eta = (\eta_1, \eta_2)$ are two parameters to be
217 estimated.

Explicitly representing spatial dependence in this way is important to accurately characterize uncertainty (e.g.Westra and Sisson (2011)), since nearby gauges often show high levels of statistical dependence. The Gaussian copula is a member of the elliptical copulas family (which also comprises the Student copula), which remains applicable to high-dimension models such as here (a region can comprise up to 16 sites, see next section) (Renard, 2011). More detailed discussions on the use of the Gaussian copula can be found in Favre et al. (2004); Renard and Lang (2007); Renard et al. (2013), and details on likelihood function computation can be found in Sun et al. (2014). We also discuss the limitation of this approach in the discussion Section 5.4.

### 2.2.2 Defining regions

Regional analyses reduce sampling uncertainty compared to at-site (local) analyses. However, to obtain the spatial pattern of the ENSO effect, regions should be neither too small nor too large: small regions may not contain enough sites to precisely estimate the model parameters, while large regions may not have a consistent association with the SOI. Therefore, we prepared 2592 gridded regions with a grid size of 5˚ by 5˚ (about 309,000 $km^2$ at the equator and 155,000 $km^2$ at 60˚N), and applied the regional model described in Section 2.2.1 to each region. Note that this regional model does not assume that the distribution of extreme precipitation is constant within each region. It only assumes that the strength of the ENSO effect and the shape parameter are constant. However, the local parameters $\boldsymbol{\theta}_{loc}^{(s)} = (\mu_{loc_0}^{(s)}, \sigma_{loc_0}^{(s)})$ enable variability in the GEV distribution within each region, with the location and scale parameters of the GEV distribution remaining site-specific.

To keep computation time feasible, we used only some of the available observation sites in a region (the computational bottleneck being the inversion of the dependence matrix $\boldsymbol{\Sigma}$). Site selection was achieved by subdividing each region into 16 sub-regions, from which the gauge with the longest record was selected if there is more than one gauge available (red dots in Figure 2). Therefore, in

each region, there were at most 16 sites used for regional analysis. We considered a region to possess enough data to apply the regional model if there were at least three sub-regions with available gauges. In total, there are 323 regions that meet the requirement of station number and record length. A justification of this way of defining regions will be described in Section 3.1.

### 2.2.3 Inference

For each region, we estimated the parameters $\theta$ in a Bayesian framework using the Markov chain Monte Carlo (MCMC) method. Relevant formulae can be found in Sun et al. (2014). In the current study, non-informative priors were used (but see Section 3.1.4 for an evaluation of an informative prior on the shape parameter). More details about the MCMC sampler are described by Renard et al. (2006a). To ensure convergence, we ran two chains with different starting points for each region. The Gelman-Rubin (GR) index (Gelman and Rubin, 1992) was used, and the MCMC sampling was considered as convergent when the GR value was less than 1.2 for all parameters. Note that the use of Bayesian inference allows the effect of sampling uncertainty to be quantified for all inferred quantities. The results are therefore not restricted to point-estimates of quantities such as the ENSO effect, conditional quantiles, and so on, but also encompass the associated uncertainties.

The Bayesian approach is not the only possible way to estimate parameters and their uncertainties. Likelihood-based methods (Bayesian or maximum likelihood) are generally favored over moment-based methods when covariates are used in the model as done here: indeed, the inclusion of the covariates in the likelihood function is quite straightforward, while deriving theoretical moments for given realizations of the covariates is more challenging. Maximum likelihood estimation techniques could also be used to estimate parameters and their uncertainty (e.g. using asymptotic Gaussian approximations or bootstrap, see Frey and Burmaster (1999)). However, we favored the Bayesian framework because it could be more adapted for future improvements of the statistical model we

consider (e.g. using region-specific priors, hierarchical modeling, etc.). This will be further discussed in section 5.4.

### 2.2.4 The effect of ENSO on precipitation quantiles

The effect of ENSO on precipitation quantiles is presented by calculating the slope of the SOI-quantile relationship. More precisely, for a given exceedance probability 1-$\alpha$, the associated quantile $q_\alpha$ is computed through the inverse function of Eq. (1):

$$q_\alpha = \frac{\sigma}{\xi} K_\alpha + \mu \tag{5}$$

where $K_\alpha = 1 - \left(-\log(\alpha)\right)^{\xi}$.

By applying Eq. (3) to each D-parameter conditional on a specific SOI value, the quantile $q_\alpha$ of site *s* becomes:

$$q_\alpha(s) = \mu_{loc_0}^{(s)} + \frac{\sigma_{loc_0}^{(s)}}{\xi_{reg}} K_\alpha + slp_\alpha * SOI \tag{6}$$

where $slp_\alpha = \begin{cases} \mu_{reg_1}^{-} + \frac{\sigma_{reg_1}^{-}}{\xi_{reg}} K_\alpha ; SOI < 0 \\ \mu_{reg_1}^{+} + \frac{\sigma_{reg_1}^{+}}{\xi_{reg}} K_\alpha ; SOI > 0 \end{cases}$ is the slope of the quantile with respect to the SOI. Note that as the slope $slp_\alpha$ only depends on the regional parameters, it is itself regional and hence does not depend on site *s* within a given region.

## 3 MODEL ILLUSTRATION AND VERIFICATION

To assess the validity of the main model assumptions and to verify that the strategy used to define regions and to select the stations within each region is relevant, we start our analysis by focusing on a particular region. We consider a region at mid to low latitude with a relatively large geographic

area to verify whether using sixteen stations is enough to obtain stable estimates. According to the coverage and availability of the data, we select the region at 32.5N 100W in Southern US (Figure 2).

## 3.1 Model demonstration for a particular region

### 3.1.1 Goodness of fit

We applied the regional model described in Eq. (3) to the DJF maximum precipitation of the sixteen stations shown as red dots in Figure 2. The goodness-of-fit of the time-varying GEV distribution can be verified through a probability-probability plot (pp-plot). For a given site *s*, the pp-plot is obtained by computing the cdfs $\left\{\hat{G}_{s,t}\left(y(s,t)\right)\right\}_{t=1,n}$ where *t* indicates the time step, $\hat{G}_{s,t}$ is the cdf of the estimated time-varying GEV at time *t*, and $y(s,t)$ is the corresponding observation. For a good fit, these cdf values should be realizations from Unif[0,1] distribution, yielding a pp-plot close to the diagonal (see e.g. Renard et al. (2013) and Sun et al. (2014) for more details). Figure S1 (a) shows a good fit for most stations. To further verify the goodness-of-fit, a Kolmogorov-Smirnov test (KS-test) at 0.05 level was used to test the distribution of the cdf values for all sixteen stations against a Unif[0,1] distribution. No significant departure from uniformity was detected, indicating that the model provides an acceptable fit to the observations.

### 3.1.2 Gaussian copula and exponential dependence-distance model

With the Gaussian copula, the spatial dependence is described through Gaussian-transformed data, where the observation is firstly transformed to a probability by applying the cumulative density function of the marginal GEV distribution, followed by the application of the quantile function of standard Gaussian distribution to obtain the Gaussian-transformed data (see Renard et al. (2013) for the details of data transformation). The empirical dependence of two stations is described by the

Pearson correlation coefficient of the Gaussian-transformed data. Figure S1(b) shows the dependence-distance relationship for the Gaussian-transformed data.

The pairwise Pearson correlations of the observed data show that for the distance of 300 km, the correlation is about 0.4, which corresponds to a rather large decorrelation distance, suggesting that the daily extreme precipitation in this region is created by large-scale atmospheric systems. If this correlation is ignored, the information content of the data will be over-estimated and the uncertainty will be under-estimated. The red lines in Figure S1(b) show that the exponential model (Eq.(4)) gives a reasonable approximation of the shape of the dependence-distance relationship. The assumption that the dependence between stations is explained by inter-station distance alone may require further enhancements in some regions (e.g. in mountainous/coastal areas, elevation/distance from coast may also be important) – this is discussed in Section 5.4. However, incorporating some form of spatial dependence still constitutes an improvement over the standard approach that ignores spatial dependence.

### 3.1.3 Stations selection

This section assesses whether using 16 stations provides sufficient data to precisely estimate the parameters of the regional model. To this end, we sort the 16 stations in descending order according to their record length, and run the same regional model by using between one to sixteen stations, and compare the posterior distribution of the regional parameters ( $\mu_{reg_1}^{-}$, $\mu_{reg_1}^{+}$ and $\xi$ ) using box plots. Figure S2 shows that when the number of stations is less than three, the posteriors distributions have low precision (large uncertainties). As the number of stations increases, the precision increases (smaller uncertainties), which highlights the advantage of regional analysis compared with local (single station) analysis on providing more precise estimates. When the number of stations is larger than ten, the posterior distributions stabilize, with the boxplots showing

very little change both in terms of location and width. This stabilization of the posterior distribution highlights the advantage of modelling spatial dependence: indeed, if the spatial dependence was ignored, each new station would be considered as bringing a similar amount of information, and the estimation uncertainty would mistakenly continue to decrease when the number of stations increases.

The analysis outlined above was repeated for 1-2 regions in each continent using all available data from those regions, and the results were consistent (not shown). Overall, this highlights two key points: (1) a minimum of approximately three stations is required; and (2) the additional information gain from including more than ten stations in the analysis is fairly limited. Given that the computation burden increases with the number of stations (due to inversion of the covariance matrix), a maximum of sixteen stations was chosen for the remaining analysis of this study.

### 3.1.4 GEV shape parameter

As the shape parameter is usually difficult to estimate, some expert prior can be used for this parameter. For example, Martins and Stedinger (2000) proposed a Gamma(6,9) distribution (referred to henceforth as the 'MS prior') as a general-purpose prior for the shape parameter in a hydrological context. In this study, we also investigate the impact of this prior distribution by comparing estimates obtained with the MS prior and with a non-informative prior (last two boxes of Figure S2). The difference between these two estimates is very small, suggesting that the MS prior does not exert any noticeable leverage on the inference. The MS prior was originally introduced in a local analysis, and in that case expert prior information can markedly improve the estimation. However, in a regional analysis, the MS prior adds less additional information, because the information provided by several stations dominates that provided by the expert prior. We therefore retain the use of non-informative priors when applying the model to the complete dataset.

353 ### 3.2 Verification of the inference for all regions

354 The analysis exemplified in section 3.1 has to be repeated for more than 300 regions, but it is not
355 feasible to manually scrutinize all regions with such a high level of detail. This section therefore
356 describes indicators aimed at verifying that the inference results remain reasonable on the whole
357 dataset.

358

359 Over the 323 regions meeting the data requirement, we first excluded the dry regions with mostly
360 zero values for seasonal maximum precipitation. Then, we estimated the model parameters (Eq.(3))
361 in all remaining regions (see Table 1). Goodness-of-fit was assessed with a KS test (0.05 level)
362 applied on each site. Since the test is repeated for all stations within a given region, we expect to
363 reject the "good-fit" assumption in a percentage of sites close to the error level of the test. It is
364 therefore necessary to assess significance at the regional scale, i.e. to determine which sites show a
365 poor fit, knowing that the local tests have been repeated over all sites of the region. To this end, we
366 used the false discovery rate (FDR) procedure (Benjamini and Hochberg, 1995). Given a regional
367 significance level, we calculated the FDR probability for each region based on the *p* values of local
368 tests. A region is considered to have a "poor-fit" if the *p* value of any local test is smaller than the
369 FDR probability. A more detailed description of the FDR procedure in the hydro-climate context is
370 given by Ventura et al. (2004) and Renard et al. (2008). Table 1 shows that the goodness of fit is
371 acceptable in more than 99% of the regions for a regional significance level of 0.05.

372

373 To check the performance of the Gaussian copula in modelling spatial correlation, we can verify
374 whether it provides a better estimation of joint probabilities of exceedances than an equivalent
375 model that ignores spatial dependence. We therefore compute the probability of a station pair
376 jointly exceeding the $75^{th}$ percentile of the at-site historical seasonal maximum daily precipitation
377 among the stations in a region. We repeatedly calculated this probability for all effective station

pairs (defined as a pair with their inter-site distance smaller than 200 km and with at least 20 common years without missing values) with both models over all regions. Figure S3 shows the scatterplot of this probability and it indicates that the exceedance probability calculated by the Gaussian copula model is mostly consistent with the empirical probability, while the model ignoring the spatial dependence tends to under-estimate the joint exceedance probability when it becomes large. Therefore, the Gaussian copula model has a better performance than the model ignoring spatial dependence.

## 4 RESULTS

In this section, we first describe the results of the parameter inference (Section 4.1). Section 4.2 then describes the effect of ENSO on precipitation quantiles. Section 4.3 discusses the seasonal effect of ENSO and Section 4.4 presents the asymmetric effect of ENSO.

### 4.1 Regional parameter estimates

In the piecewise linear model proposed in Eq.(3), slope regression parameters $\mu_{reg_1}^{-}$ and $\sigma_{reg_1}^{-}$ ($\mu_{reg_1}^{+}$ and $\sigma_{reg_1}^{+}$) characterize the effect of El Niño (La Niña) on the location and scale parameters. If the effect is significant, the posterior distribution of $\mu_{reg_1}^{-}$ and/or $\sigma_{reg_1}^{-}$ ($\mu_{reg_1}^{+}$ and/or $\sigma_{reg_1}^{+}$) should be significantly different to zero.

Figure 3 illustrates significance and intensity for $\mu_{reg_1}^{-}$ (El Niño) and $\mu_{reg_1}^{+}$ (La Niña) for each region during DJF. The location parameter increases during a El Niño phase in central and southern North America, southeast South America, southeast China and northern Europe, and decreases in western North America and northern Southeast Asia, and more weakly in South Africa. Conversely, the location parameter increases during a La Niña phase in central North America, northern Southeast

Asia, South Africa, Australia and northern Europe, and decreases in southern North America and the northern India subcontinent.

This global pattern for both phases is consistent with the results of Kenyon and Hegerl (2010) for their November to April season. However, since their study was based on at-site (local) analysis, the significance of the ENSO effect in their results was lower. Our result is also consistent with the ENSO-precipitation teleconnection identified in several regional studies: North America (Castello and Shelton, 2004; Cayan et al., 1999); South America (Grimm and Tedeschi, 2009); eastern China (Wu et al., 2003); and Australia (Cai et al., 2010; King et al., 2013).

The effect of ENSO on the scale parameter (Figure 4) is also significant in many places, although less than for the location parameter. This important result suggests that ENSO not only shifts the distribution of extremes, but also modifies its variability. In general, for the areas where the effect of ENSO is strong on the location parameter, a similar effect is found on the scale parameter (e.g. southeast China and southeast South America during El Niño; and northern Southeast Asia and Australia during La Niña).

According to the spatial pattern of the ENSO effect and the availability of data, nineteen areas are defined (Figure 1), with areas 1-4 in Central and North America (Group I), 5-8 in Europe (Group II), 9-13 in Asia (Group III), and 14-19 covering the Southern Hemisphere (Group IV). Table 2 summarizes the results discussed above for DJF, and also for the three other seasons whose results are not reported in full detail here. It indicates that DJF is the season with the strongest ENSO effect. More detailed results on the seasonality of ENSO effects will be discussed in Section 4.3.

## 4.2 The effect of ENSO on precipitation quantiles

A more impact-oriented picture of the effect of ENSO on extreme precipitation can be obtained by expressing it in terms of quantiles rather than in terms of location and scale parameters, as this quantity provides direct information on the likely implications of ENSO on hydrologic hazard. We now show the percentage change in 1 in 10 year DJF precipitation during a strong El Niño or La Niña phase and a neutral phase. The 1 in 10 year precipitation intensity (0.9 quantile) is computed from Eq. (6) with $\alpha$ equal to 0.1, which requires the use of local regression parameters ($\mu_{loc_0}^{(s)}$ and $\sigma_{loc_0}^{(s)}$). Consequently, the estimates from the regional model in terms of quantile change cannot be shown at the scale of regions, but instead has to be shown for all sites. Moreover, note that we can derive the full posterior distribution of this percentage change by propagating all MCMC-generated parameters through Eq. (6).

Figure 5 illustrates the percentage change for 1 in 10 year precipitation during DJF between an extreme ENSO event (|SOI| = 20) and a neutral phase (SOI = 0). The percentage changes in Figure 5 correspond to the posterior median. Red (blue) indicates that extreme El Niño/La Niña increases (decreases) the 1 in 10 year precipitation intensity. During a strong El Niño event, the 1 in 10 year precipitation can increase by 20% to 50% in southern North America and southeast China, about 40% in southeast South America, and 10% to 20% in central North America. A decrease of 10% can be observed in western North America and 10% to 20% in northern Southeast Asia.

During a strong La Niña episode, the 1 in 10 year precipitation increases (relative to neutral conditions) by about 80% in southwest Western Australia, 40% in eastern Australia, 20% in southern Australia and northeast China, 10% in northern Southeast Asia, central North America and northern Europe, and 10% to 40% (from east to west) in South Africa. However, the intensity of the

1 in 10 year precipitation decreases in southern North America (about 50% in Mexico) and northern India (about 20%). Further investigation on the 80% increase in southwest Western Australia reveals that DJF is not the main precipitation season, thus the absolute increase in annual maximum precipitation is actually not large. However, a 40% increase in eastern Australia will correspond to much larger absolute increases in extreme precipitation, which may lead to societally important events such as the Queensland flood in 2010-2011 (Cai and van Rensch, 2012).

### 4.3 Seasonality of the effect of ENSO on extreme precipitations

The results shown in Figure 5 can be further summarized to get an overview of the ENSO effect for all four seasons. This is achieved as follows: the percentage changes shown in Figure 5 for individual stations are summarized as boxplots for each of the 19 areas defined in Figure 1 and for each season. This yields the synthetic representation shown in Figure 6. Note that in this figure, boxplots represent the range of quantile changes from individual gauges within each area. However, the sampling uncertainty in quantile change estimates is ignored in this representation. Consequently, the boxplots should not be interpreted in terms of assessing the statistical significance of quantile changes. However, as a reminder of this sampling variability, we highlight in bold the seasons with moderate or strong ENSO effect as given by Table 2. If the box does not encompass the zero value, it means that ENSO has potential effects over the area, however it still needs to be confirmed through Table 2. Sometimes the box contains the zero value but the effect of ENSO for that season is moderate or strong; this means that significant ENSO effects are only detected in a sub-area rather than the whole area. Table 3 qualitatively summarizes the main areas and seasons affected by ENSO with the consideration of both Table 2 and Figure 6.

In general, DJF is the season with the strongest ENSO effect, and JJA is the season with the weakest effect for both phases. For the El Niño phase, positive effects are mainly found in central

and southern North America, southeast and northeast China, and southeast South America during DJF and surrounding seasons, while negative effects are mainly found in southern and eastern Australia during SON. For the La Niña phase, positive effects are mainly found in western Pacific areas (eastern Asia and Australia) in DJF and surrounding seasons. However, La Niña effects are not very consistent in eastern Pacific areas: positive effects are found in central and western North America in SON, and negative effects are found in southern North America and southeast South America, but in different seasons.

It is not surprising that the strongest ENSO effects are found in the Pacific areas, especially in the tropical zone. However, to a lesser extent, ENSO also affects northern Europe during DJF for both phases, and the eastern Mediterranean during SON for El Niño. The Indian subcontinent is also affected during the La Niña phase, with the northern and southern parts having different effects in different seasons.

### 4.4 Asymmetric behavior of ENSO on extreme precipitations

The use of a different linear function in the El Niño and La Niña phases enables the modelling framework to capture and evaluate the asymmetric impact of the ENSO-precipitation relationship. It provides the flexibility to assess at each site whether each ENSO phase can have a positive, negative or no effect on extreme precipitation. If the parameters quantifying the ENSO effect on the location and/or scale parameters are the same in each phase (i.e. $\mu_{reg_1}^{-} = \mu_{reg_1}^{+}$ and/or $\sigma_{reg_1}^{-} = \sigma_{reg_1}^{+}$), this is a symmetric relationship (often assumed in previous studies) and corresponds to observing opposite effects in the two phases (e.g. precipitation decreases during El Niño but increases during La Niña) (see Figure 7(a)). Conversely, asymmetric behavior corresponds to having non-opposite effects during El Niño and La Niña. The parameters governing the ENSO effect on the location and/or scale parameters are hence different in each phase (i.e. $\mu_{reg_1}^{-} \neq \mu_{reg_1}^{+}$ and/or $\sigma_{reg_1}^{-} \neq \sigma_{reg_1}^{+}$).

There are two 'types' of asymmetric behavior: (i) One-phase: no effect for one phase and a strong effect for the other phase. Figure 7(b) shows an example of having strong positive effect during La Niña, but no effect during El Niño. (ii) Two-phase: strong, but non-opposite ENSO effects during both El Niño and La Niña phases. Figure 7(c) shows an example of having strong positive effect during both El Niño and La Niña.

The last column of Table 3 summarizes the asymmetric nature of the ENSO-extreme precipitation relationship during the season with the strongest effect. In most areas, precipitation is only affected during one phase of ENSO, which corresponds to an asymmetric behavior. Two-phase asymmetric behavior is found in central and western North America, northeast China and northern Europe, where the 10-year precipitation is increased during both strong El Niño and La Niña events (relative to a neutral phase SOI=0). Symmetric behavior is found in southern US during DJF, southern and eastern Australia during SON, and northern Southeast Asia during DJF and SON, where effects of opposite sign are found during two phases.

# 5 DISCUSSION

## 5.1 Practical implications

In the perspective of engineering design and operations, knowledge of how the extreme events change based on ENSO can enable planners to prepare strategies for early response based on ENSO forecast. At a large scale, this information is more important for government officers and policy designers to evaluate in advance the population and potential economic losses associated with the projected flood risk, and to prepare mitigation measures.

The results of this study have significant practical implications because they provide quantitative estimates of the percentage change in extreme daily precipitation intensity for a unit change in the SOI. Given that ENSO forecasts show some skill at monthly to seasonal lead times (e.g. Jin et al. (2008)), it is possible to use this information to provide quantitative seasonal forecasts of extreme precipitation. From an engineering standpoint, this provides opportunities to improve the management of water resource risks: for instance, dam operation could use the forecasted ENSO state to optimize hydroelectricity production while enforcing appropriate precautionary measures to mitigate flood risk (see e.g. Lima and Lall (2010a)). Another key outcome of this study is the identification of regions with an asymmetric ENSO-precipitation relationship (Table 3 and Figure 6). It is possible that current approaches to estimate extreme precipitation quantiles in these regions (which either ignore ENSO or use the symmetric assumption) under-estimate extreme precipitation quantiles. This has practical implications for the design and management of flood-sensitive infrastructure in these regions.

### 5.2 Changes in ENSO teleconnections

For the more distant future, an important question in terms of ENSO is how the evolution of such an influential global process will affect extreme precipitation in a future climate. Several challenges need to be met to address this issue. Firstly, GCM simulations suggest the possible occurrence of "super-ENSO" events (Latif et al., 2013) in the future, which may require extrapolating from the regional model used in this study well beyond the range of observed SOI values. Whether or not the "piecewise linear" relationship used in this model can be extrapolated to very high SOI values is an open question. Secondly, the ability of GCMs to describe the frequency characteristics (e.g. Johnson et al. (2011) ) and the physical mechanisms governing the development of ENSO events remains limited, as discussed, for example, by Bellenger et al. (2013). Note that an interesting potential application of our statistical model would be to apply it to both GCM outputs and

observations to assess the ability of GCMs to reproduce the ENSO-extreme precipitation teleconnection and better understand the physical drivers of the asymmetric ENSO-precipitation relationship. This would help evaluate whether projections of future ENSO events can be reliably used to deduce the evolution of extreme precipitation in a future climate.

### 5.3 Reliability of the definition of a region

An important contribution of this study is the use of a regional statistical model. Indeed, given the available record length and the large local variability of extreme precipitation, a precise quantification of the ENSO effect on extreme precipitation is difficult to achieve without regionalization. The price to pay is the requirement to define homogenous regions. In this study, we defined the regions as grid cells, i.e. according to latitude and longitude only. By repeatedly applying the regional model over geographic regions covering all land areas with available data, the approach has proved a good compromise for the 'bias-variance' trade-off. In other words, compared with at-site analysis, the uncertainties are much smaller; compared with global analysis, regional features can still be highlighted.

It is important to note that for the purposes of the current study only the shape parameter and the ENSO effect parameters are regional. Other parameters are site-specific, which provides the flexibility to account for between-site differences within the region. However, the definition of homogeneous regions adopted in this paper might remain unduly simplistic for some geographical areas. In mountainous areas, in particular, orographic influences can lead to substantial differences in precipitation patterns across small spatial areas. For example, because of the Andes Mountains, precipitation within the grid cells defined across Chile and Argentina may be caused by very different circulation patterns, which are not affected in the same way by ENSO. Thus, assuming the same effect of ENSO in these regions is questionable. A possible solution is to redefine regions by

565 subdividing the grid cells into smaller grids. However, the number of available observation sites
566 might be too low for a meaningful regional analysis. A better outcome might be achieved if the
567 homogeneous regions were based on climate or physiographic variables, or the data characteristics
568 (Bernard et al., 2013; Sun et al., 2015), as opposed to the simple regular grid adopted here.
569 However this requires an understanding of the key driving factors that can lead to precipitation
570 variability in a given area, which are likely to be complex and spatially heterogeneous, and will
571 probably differ depending on the region being analyzed.

572 **5.4 Potential extensions of the statistical model**

573 In addition to improving the definition of regions, several avenues can be identified to extend the
574 statistical model itself. In this discussion, we focus on improving prior specification, using
575 hierarchical models and refining the treatment of spatial dependence.

576 The Bayesian approach has a long history in frequency analysis of both extreme precipitation and
577 floods (e.g. Kuczera, 1999; Vicens et al., 1975; Wood and Rodr ǵuez-Iturbe, 1975a,b). One of its
578 key strengths is the ability to augment the information in the data with additional prior information.
579 For instance, O'Hagan et al. (2006) and Denham and Mengersen (2007) describe general techniques
580 to elicit expert knowledge in the form of a prior distribution, while Viglione et al. (2013) discuss the
581 importance of prior information for flood frequency analysis. In this paper, we used non-
582 informative priors and therefore did not take advantage of this strength of Bayesian estimation. We
583 trialed the use of the general-purpose Martin and Stedinger's prior for the shape parameter (see
584 Section 3.1.4) but it did not bring any noticeable information beyond that already contained in the
585 regional dataset. Further development of appropriate region specific priors by careful investigation
586 of each region's characteristics (e.g. climate and topography) may improve the parameter estimation,
587 in particular for regions with scarce observations.

An additional avenue to improve the statistical model is to add some hierarchical component(s) to the model, which can be done naturally in a Bayesian framework. In particular, the current model cannot be used for estimation at ungauged sites due to the existence of local parameters, whose values are site-specific. This could be remedied by using a regression approach to link the values of local parameters with site characteristics such as elevation and distance to sea. A hierarchical modeling approach could then be used to include this regression model, as described by e.g. Cooley et al. (2005) and Renard (2011). Alternatively, the flexibility of the model could be enhanced by allowing ENSO effects to vary in space, but in a smooth way. This can also be achieved with a hierarchical component that would constrain the spatial variations of ENSO effects to follow a chosen spatial hyper-distribution.

Finally, the treatment of spatial dependence could also be refined in at least two ways. The first is to refine the dependence-distance relationship of Eq.(4), by moving beyond the Euclidean distance to explain spatial dependence. In particular, orographic effects are likely to play an important role in some regions, and they could be included in the spatial dependence model (see for instance Blanchet and Davison (2011) in the context of a snow depth variable). A second way is to replace the Gaussian copula with another model of spatial dependence. For instance, the Student copula (another member of the Elliptical copula family) could be used to account for asymptotic dependence. Alternative approaches include pair-copula models (Gräler and Pebesma, 2011) or max-stable models (e.g. Westra and Sisson (2011) and Ribatet et al. (2012)). We stress however that the data selection procedure adopted in this paper limits the amount of spatial dependence: the selection of a single site for each of the 16 sub-regions within a region (see section 2.2.2 and Figure 2) avoids the selection of many close, highly-dependent pairs of sites. In this context, a Gaussian copula may be sufficient as a first-order approximation to capture the dependence observed in the data. In other contexts (e.g. more highly-dependent pairs of sites, or necessity to extrapolate the

dependence structure well beyond observed levels), a finer treatment of spatial dependence may be required.

### 5.5 Impact of other large scale modes of climate variability

Besides ENSO, other large scale modes of climate variability could also affect regional extreme precipitation. For instance, the Indian Ocean Dipole (IOD) affects the precipitation in northern Southeast Asia and Australia, and the North Atlantic Oscillation influences precipitation in North America and Europe. Research also indicates that in many regions, precipitation is influenced by the combined effect of distinct large scale modes (e.g., Keim and Verdon-Kidd (2009); the IOD and ENSO both influence precipitation in Australia.) However, the ways in which the two modes combine to influence extreme precipitation at the global scale requires further investigation.

The current study was a purely statistical analysis of the effect of ENSO on extreme precipitation, and does not provide any indication on the physical mechanisms governing such climate-precipitation teleconnections. If such a physical mechanism could be understood, it might lead to a more physically-based regression model structure (rather than the piecewise linear model adopted in this study) to provide a better evaluation of the ENSO effect on extreme precipitation.

## 6 CONCLUSIONS

We applied a climate-informed regional frequency analysis framework to describe the global pattern of the effect of ENSO on extreme precipitation, focusing particularly on extreme quantiles. The ENSO effects over many regions are quantified along with associated uncertainties. This study goes beyond merely studying the relationship between ENSO and “extreme” precipitation indices, and is extended to more ‘design-relevant’ extreme events (e.g. 1 in 10 year precipitation). The

technique of regionalizing the ENSO effects significantly strengthens our ability to quantify such effects.

Keeping in mind the limitation of the HadEx2 data set (whose uneven spatial sampling favors temperate climates), we draw the following conclusions from the analyses carried out in this paper:(i) ENSO significantly affects extreme precipitation across large parts of the world, which are not limited to Pacific areas; (ii) the ENSO effect varies substantially by season, but DJF is in general the season with the strongest ENSO effect, with the greatest changes, up to 50% higher or lower, in the 1 in 10 year precipitation quantiles between a strong El Niño/La Niña event (|SOI=20|) and a neutral phase (SOI=0); and (iii) the relationship is asymmetric. In most places, extreme precipitation is significantly influenced during only one phase. Two-phase asymmetry (with strong but non-opposite effects during El Niño and La Niña) is also found in several areas, e.g. central North America and northeast China. In contrast, a symmetric behavior is only found in southern US during DJF, southern and eastern Australia during SON, and northern Southeast Asia during DJF and SON.

## 7 ACKNOWLEDGEMENTS

We wish to acknowledge Dr Lisa Alexander who provided us with the global observed extreme precipitation HadEx2 dataset. This data set is now available at http://www.climdex.org/index.html. We wish to acknowledge Prof. Dmitri Kavetski for providing the FORTRAN library DMSL. Rfortran software library (Thyer et al., 2011) is used for the data and commands transfer between FORTRAN and R. Dr Westra's time was supported by Australian Research Council (ARC) Discovery project DP150100411. We also wish to acknowledge the research funding provided by Electricité de France (EDF), Irstea DRI, Région Rhône-Alpes (Explora'doc), the University of Adelaide (through ARC Discovery Project DP1094796) and the American International Group (CU12-2326).

658

# 8 REFERENCES

Ahern, M., Kovats, R.S., Wilkinson, P., Few, R., Matthies, F., 2005. Global health impacts of floods: Epidemiologic evidence. Epidemiologic Reviews, 27: 36-46.

Alexander, L.V., Uotila, P., Nicholls, N., 2009. Influence of sea surface temperature variability on global temperature and precipitation extremes. Journal of Geophysical Research-Atmospheres, 114. DOI:10.1029/2009jd012301

Aryal, S.K. et al., 2009. Characterizing and modeling temporal and spatial trends in rainfall extremes. Journal of Hydrometeorology, 10(1): 241-253.

Bellenger, H., Guilyardi, E., Leloup, J., Lengaigne, M., Vialard, J., 2013. ENSO representation in climate models: from CMIP3 to CMIP5. Climate Dynamics: 1-20. DOI:10.1007/s00382-013-1783-z

Benjamini, Y., Hochberg, Y., 1995. Controlling the False Discovery Rate: A Practical and Powerful Approach to Multiple Testing. Journal of the Royal Statistical Society. Series B (Methodological), 57(1): 289-300. DOI:10.2307/2346101

Bernard, E., Naveau, P., Vrac, M., Mestre, O., 2013. Clustering of maxima: Spatial dependencies among heavy rainfall in France. Journal of Climate, 26(20): 7929-7937.

Blanchet, J., Davison, A.C., 2011. Spatial Modeling of Extreme Snow Depth. Ann Appl Stat, 5(3): 1699-1725. DOI:Doi 10.1214/11-Aoas464

Cai, W., Cowan, T., 2009. La Nina Modoki impacts Australia autumn rainfall variability. Geophysical Research Letters, 36. DOI:Artn L12805

Doi 10.1029/2009gl037885

Cai, W., van Rensch, P., 2012. The 2011 southeast Queensland extreme summer rainfall: A confirmation of a negative Pacific Decadal Oscillation phase? Geophys Res Lett, 39. DOI:10.1029/2011gl050820

Cai, W., van Rensch, P., Cowan, T., Sullivan, A., 2010. Asymmetry in ENSO teleconnection with regional rainfall, its multidecadal variability, and impact. Journal of Climate, 23(18): 4944-4955. DOI:10.1175/2010jcli3501.1

Castello, A.F., Shelton, M.L., 2004. Winter precipitation on the US Pacific Coast and El Nino Southern oscillation events. International Journal of Climatology, 24(4): 481-497. DOI:10.1002/joc.1011

Cayan, D.R., Redmond, K.T., Riddle, L.G., 1999. ENSO and hydrologic extremes in the western United States. Journal of Climate, 12(9): 2881-2893. DOI:10.1175/1520-0442(1999)012<2881:eaheit>2.0.co;2

Chen, J.M., Li, T., Shih, C.F., 2008. Asymmetry of the El Nino-spring rainfall relationship in Taiwan. J. Meteorol. Soc. Jpn., 86(2): 297-312. DOI:10.2151/jmsj.86.297

Coles, S., 2001. An introduction to statistical modeling of extreme values, 208. Springer, London.

Coles, S., Pericchi, L.R., Sisson, S., 2003. A fully probabilistic approach to extreme rainfall modeling. Journal of Hydrology, 273(1-4): 35 - 50.

Cooley, D., Nychka, D., Naveau, P., 2005. A spatial Bayesian hierarchical model for a precipitation return levels map. Extreme value analysis, Gothenburg, Sweden.

Curtis, S. et al., 2007. Precipitation extremes estimated by GPCP and TRMM: ENSO relationships. Journal of Hydrometeorology, 8(4): 678-689. DOI:10.1175/jhm601.1

Dai, A., Fung, I.Y., DelGenio, A.D., 1997. Surface observed global land precipitation variations during 1900-88. Journal of Climate, 10(11): 2943-2962. DOI:Doi 10.1175/1520-0442(1997)010<2943:Soglpv>2.0.Co;2

Dai, A., Wigley, T.M.L., 2000. Global patterns of ENSO-induced precipitation. Geophys Res Lett, 27(9): 1283-1286. DOI:Doi 10.1029/1999gl011140

Denham, R., Mengersen, K., 2007. Geographically assisted elicitation of expert opinion for regression models. Bayesian Analysis, 2(1): 99-135.

Donat, M.G. et al., 2013. Updated analyses of temperature and precipitation extreme indices since the beginning of the twentieth century: The HadEX2 dataset. Journal of Geophysical Research: Atmospheres, 118(5): 2098-2118. DOI:10.1002/jgrd.50150

Favre, A.C., El Adlouni, S., Perreault, L., Thiemonge, N., Bobee, B., 2004. Multivariate hydrological frequency analysis using copulas. Water Resources Research, 40(1): W01101.

Feng, J., Li, J.P., 2011. Influence of El Nino Modoki on spring rainfall over south China. Journal of Geophysical Research-Atmospheres, 116. DOI:Artn D13102

Doi 10.1029/2010jd015160

Fernandez, H.W., Fernandez, B., 2002. The influence of ENSO in the precipitation regime in southern South America. Ingenieria Hidraulica En Mexico, 17(3): 5-16.

Fisher, R.A., Tippett, L.H.C., 1928. Limiting forms of the frequency distribution of the largest or smallest member of a sample. Mathematical Proceedings of the Cambridge Philosophical Society, 24(02): 180-190.

713 Frey, H.C., Burmaster, D.E., 1999. Methods for characterizing variability and uncertainty: comparison of bootstrap
714 simulation and likelihood-based approaches. Risk Analysis, 19(1): 109-130.
715 Gelman, A., Rubin, D.B., 1992. Inference from iterative simulation using multiple sequences. Statistical science, 7:
716 457-472.
717 Gershunov, A., Barnett, T.P., 1998. ENSO influence on intraseasonal extreme rainfall and temperature frequencies in
718 the contiguous United States: Observations and model results. Journal of Climate, 11(7): 1575-1586.
719 DOI:10.1175/1520-0442(1998)011<1575:eioier>2.0.co;2
720 Gräler, B., Pebesma, E., 2011. The pair-copula construction for spatial data: a new approach to model spatial
721 dependency. Procedia Environmental Sciences, 7: 206-211.
722 Grimm, A.M., 2011. Interannual climate variability in South America: impacts on seasonal precipitation, extreme
723 events, and possible effects of climate change. Stochastic Environmental Research and Risk Assessment,
724 25(4): 537-554. DOI:10.1007/s00477-010-0420-1
725 Grimm, A.M., Tedeschi, R.G., 2009. ENSO and extreme rainfall events in South America. Journal of Climate, 22(7):
726 1589-1609. DOI:10.1175/2008jcli2429.1
727 Hanel, M., Buishand, T.A., Ferro, C.A.T., 2009. A nonstationary index flood model for precipitation extremes in
728 transient regional climate model simulations. Journal of Geophysical Research-Atmospheres, 114. DOI:Artn
729 D15107
730 Doi 10.1029/2009jd011712
731 Hannachi, A., 2001. Toward a nonlinear identification of the atmospheric response to ENSO. Journal of Climate, 14(9):
732 2138-2149. DOI:10.1175/1520-0442(2001)014<2138:taniot>2.0.co;2
733 Higgins, R.W., Kousky, V.E., Xie, P., 2011. Extreme precipitation events in the south-central United States during May
734 and June 2010: Historical perspective, role of ENSO, and trends. Journal of Hydrometeorology, 12(5): 1056-
735 1070. DOI:10.1175/jhm-d-10-05039.1
736 Hoerling, M.P., Kumar, A., Xu, T.Y., 2001. Robustness of the nonlinear climate response to ENSO's extreme phases.
737 Journal of Climate, 14(6): 1277-1293. DOI:10.1175/1520-0442(2001)014<1277:rotncr>2.0.co;2
738 Hoerling, M.P., Kumar, A., Zhong, M., 1997. El Nino, La Nina, and the nonlinearity of their teleconnections. Journal of
739 Climate, 10(8): 1769-1786. DOI:10.1175/1520-0442(1997)010<1769:enolna>2.0.co;2
740 Jin, E. et al., 2008. Current status of ENSO prediction skill in coupled ocean–atmosphere models. Climate Dynamics,
741 31(6): 647-664. DOI:10.1007/s00382-008-0397-3
742 Johnson, F., Westra, S., Sharma, A., Pitman, A.J., 2011. An assessment of GCM skill in simulating persistence across
743 multiple time scales. Journal of Climate, 24(14): 3609-3623. DOI:10.1175/2011JCLI3732.1
744 Jones, C., Carvalho, L.M.V., 2012. Spatial-intensity variations in extreme precipitation in the Contiguous United States
745 and the Madden-Julian Oscillation. Journal of Climate, 25(14): 4898-4913. DOI:10.1175/jcli-d-11-00278.1
746 Kane, R.P., 1999. El Nino timings and rainfall extremes in India, Southeast Asia and China. International Journal of
747 Climatology, 19(6): 653-672. DOI:10.1002/(sici)1097-0088(199905)19:6<653::aid-joc379>3.3.co;2-3
748 Katz, R.W., Parlange, M.B., Naveau, P., 2002. Statistics of extremes in hydrology. Advances in Water Resources, 25(8-
749 12): 1287 - 1304.
750 Kayano, M.T., Andreoli, R.V., 2006. Relationships between rainfall anomalies over northeastern Brazil and the El
751 Nino-Southern Oscillation. Journal of Geophysical Research-Atmospheres, 111(D13).
752 DOI:10.1029/2005jd006142
753 Keim, A.S., Verdon-Kidd, D.C., 2009. Climatic drivers of Victorian streamflow: Is ENSO the dominant influence?
754 Australian Journal of Water Resources, 13(1): 17.
755 Kenyon, J., Hegerl, G.C., 2010. Influence of modes of climate variability on global precipitation extremes. Journal of
756 Climate, 23(23): 6248-6262. DOI:10.1175/2010jcli3617.1
757 King, A.D., Alexander, L.V., Donat, M.G., 2013. Asymmetry in the response of eastern Australia extreme rainfall to
758 low-frequency Pacific variability. Geophys Res Lett: 1-6. DOI:10.1002/grl.50427
759 Kripalani, R.H., Kulkarni, A., 1997. Rainfall variability over South-east Asia - Connections with Indian monsoon and
760 enso extremes: New perspectives. International Journal of Climatology, 17(11): 1155-1168.
761 DOI:10.1002/(sici)1097-0088(199709)17:11<1155::aid-joc188>3.0.co;2-b
762 Kruger, A.C., 1999. The influence of the decadal-scale variability of summer rainfall on the impact of El Nino and La
763 Nina events in South Africa. International Journal of Climatology, 19(1): 59-68. DOI:10.1002/(sici)1097-
764 0088(199901)19:1<59::aid-joc347>3.3.co;2-2
765 Kuczera, G., 1999. Comprehensive at - site flood frequency analysis using Monte Carlo Bayesian inference. Water
766 Resources Research, 35(5): 1551-1557.
767 Kwon, H.-H., Khalil, A.F., Siegfried, T., 2008. Analysis of extreme summer rainfall using climate teleconnections and
768 typhoon characteristics in South Korea. J Am Water Resour As, 44(2): 436-448. DOI:10.1111/j.1752-
769 1688.2008.00173.x
770 Latif, M., Semenov, V., Wonsun, P., 2013. Super El Niños in a Warming World, EGU General Assembly Conference
771 Abstracts, pp. 5348.

Li, C., Ma, H., 2012. Relationship between ENSO and winter rainfall over Southeast China and its decadal variability. Adv Atmos Sci, 29(6): 1129-1141. DOI:DOI 10.1007/s00376-012-1248-z

Lima, C.H.R., Lall, U., 2010a. Climate informed long term seasonal forecasts of hydroenergy inflow for the Brazilian hydropower system. Journal of Hydrology, 381(1–2): 65-75. DOI:http://dx.doi.org/10.1016/j.jhydrol.2009.11.026

Lima, C.H.R., Lall, U., 2010b. Spatial scaling in a changing climate: A hierarchical bayesian model for non-stationary multi-site annual maximum and monthly streamflow. Journal of Hydrology, 383(3-4): 307-318.

Lyon, B., Barnston, A.G., 2005. ENSO and the spatial extent of interannual precipitation extremes in tropical land areas. Journal of Climate, 18(23): 5095-5109. DOI:10.1175/jcli3598.1

Mannshardt-Shamseldin, E.C., Smith, R.L., Sain, S.R., Mearns, L.O., Cooley, D., 2010. Downscaling extremes: A comparison of extreme value distributions in point-source and gridded precipitation data. The Annals of Applied Statistics: 484-502.

Martins, E.S., Stedinger, J.R., 2000. Generalized maximum-likelihood generalized extreme-value quantile estimators for hydrologic data. Water Resources Research, 36(3): 737-744. DOI:10.1029/1999WR900330

Meehl, G.A., Tebaldi, C., Teng, H., Peterson, T.C., 2007. Current and future US weather extremes and El Nino. Geophys Res Lett, 34(20). DOI:10.1029/2007gl031027

Min, S.K., Cai, W.J., Whetton, P., 2013. Influence of climate variability on seasonal extremes over Australia. Journal of Geophysical Research-Atmospheres, 118(2): 643-654. DOI:10.1002/jgrd.50164

O'Hagan, A. et al., 2006. Uncertain judgements: eliciting experts' probabilities. John Wiley & Sons.

OrtizBevia, M.J., Perez-Gonzalez, I., Alvarez-Garcia, F.J., Gershunov, A., 2010. Nonlinear estimation of El Nino impact on the North Atlantic winter. Journal of Geophysical Research-Atmospheres, 115. DOI:10.1029/2009jd013387

Ouarda, T.B.M.J., El-Adlouni, S., 2011. Bayesian nonstationary frequency analysis of hydrological variables. J Am Water Resour As, 47(3): 496-505. DOI:DOI 10.1111/j.1752-1688.2011.00544.x

Pscheidt, I., Grimm, A.M., 2009. Frequency of extreme rainfall events in Southern Brazil modulated by interannual and interdecadal variability. International Journal of Climatology, 29(13): 1988-2011. DOI:10.1002/joc.1799

Renard, B., 2011. A Bayesian hierarchical approach to regional frequency analysis. Water Resources Research, 47(11): W11513. DOI:10.1029/2010WR010089

Renard, B., Garreta, V., Lang, M., 2006a. An application of Bayesian analysis and Markov chain Monte Carlo methods to the estimation of a regional trend in annual maxima. Water Resources Research, 42(12): W12422.

Renard, B., Lang, M., 2007. Use of a Gaussian copula for multivariate extreme value analysis: Some case studies in hydrology. Advances in Water Resources, 30(4): 897-912.

Renard, B., Lang, M., Bois, P., 2006b. Statistical analysis of extreme events in a non-stationary context via a Bayesian framework: case study with peak-over-threshold data. Stochastic Environmental Research and Risk Assessment, 21(2): 97-112. DOI:DOI 10.1007/s00477-006-0047-4

Renard, B. et al., 2008. Regional methods for trend detection: Assessing field significance and regional consistency. Water Resources Research, 44(8). DOI:Artn W08419

Doi 10.1029/2007wr006268

Renard, B., Sun, X., Lang, M., 2013. Bayesian methods for non-stationary extreme value analysis. In: AghaKouchak, A., Easterling, D., Hsu, K., Schubert, S., Sorooshian, S. (Eds.), Extremes in a changing climate: Detection, analysis and uncertainty. Water Science and Technology Library. Springer Netherlands, pp. 39-95. DOI:10.1007/978-94-007-4479-0_3

Ribatet, M., Cooley, D., Davison, A.C., 2012. Bayesian inference from composite likelihoods, with an application to spatial extremes. Stat. Sin, 22(2): 813-845.

Ropelewski, C.F., Halpert, M.S., 1987. Global and regional scale precipitation patterns associated with the El-Nino Southern Oscillation. Mon Weather Rev, 115(8): 1606-1626. DOI:Doi 10.1175/1520-0493(1987)115<1606:Garspp>2.0.Co;2

Sardeshmukh, P.D., Compo, G.P., Penland, C., 2000. Changes of probability associated with El Nino. Journal of Climate, 13(24): 4268-4286. DOI:10.1175/1520-0442(2000)013<4268:copawe>2.0.co;2

Schubert, S.D., Chang, Y., Suarez, M.J., Pegion, P.J., 2008. ENSO and wintertime extreme precipitation events over the contiguous united states. Journal of Climate, 21(1): 22-39. DOI:10.1175/2007jcli1705.1

Shang, H., Yan, J., Zhang, X., 2011. El Nino-Southern Oscillation influence on winter maximum daily precipitation in California in a spatial model. Water Resources Research, 47. DOI:10.1029/2011wr010415

Sun, X., Lall, U., Merz, B., Dung, N.V., 2015. Hierarchical Bayesian clustering for nonstationary flood frequency analysis: Application to trends of annual maximum flow in Germany. Water Resources Research: (in press). http://dx.doi.org/10.1002/2015WR017117. DOI:10.1002/2015WR017117

Sun, X., Thyer, M., Renard, B., Lang, M., 2014. A general regional frequency analysis framework for quantifying local-scale climate effects: A case study of ENSO effects on Southeast Queensland rainfall. Journal of Hydrology, 512(0): 53-68. DOI:http://dx.doi.org/10.1016/j.jhydrol.2014.02.025

831 Thyer, M., Leonard, M., Kavetski, D., Need, S., Renard, B., 2011. The open source RFortran library for accessing R
832 from Fortran, with applications in environmental modelling. Environ Modell Softw, 26(2): 219-234. DOI:DOI
833 10.1016/j.envsoft.2010.05.007
834 Tramblay, Y. et al., 2012. Climate change impacts on extreme precipitation in Morocco. Global and Planetary Change,
835 82-83: 104-114. DOI:10.1016/j.gloplacha.2011.12.002
836 Vanheerden, J., Terblanche, D.E., Schulze, G.C., 1988. The Southern Oscillation and South-African Summer Rainfall. J
837 Climatol, 8(6): 577-597.
838 Ventura, V., Paciorek, C.J., Risbey, J.S., 2004. Controlling the Proportion of Falsely Rejected Hypotheses when
839 Conducting Multiple Tests with Climatological Data. Journal of Climate, 17(22): 4343-4356.
840 DOI:10.1175/3199.1
841 Vicens, G.J., Rodriguez‐Iturbe, I., Schaake, J.C., 1975. A Bayesian framework for the use of regional information in
842 hydrology. Water Resources Research, 11(3): 405-414.
843 Viglione, A., Merz, R., Salinas, J.L., Blöschl, G., 2013. Flood frequency hydrology: 3. A Bayesian analysis. Water
844 Resources Research, 49(2): 675-692.
845 Wan, S.Q., Hu, Y.L., You, Z.Y., Kang, J.P., Zhu, J.G., 2013. Extreme monthly precipitation pattern in China and its
846 dependence on Southern Oscillation. International Journal of Climatology, 33(4): 806-814.
847 DOI:10.1002/joc.3466
848 Ward, P.J., Eisner, S., Flörke, M., Dettinger, M.D., Kummu, M., 2014a. Annual flood sensitivities to El Niño–Southern
849 Oscillation at the global scale. Hydrology and Earth System Sciences, 18(1): 47-66.
850 Ward, P.J. et al., 2014b. Strong influence of El Niño Southern Oscillation on flood risk around the world. Proceedings
851 of the National Academy of Sciences, 111(44): 15659-15664. DOI:10.1073/pnas.1409822111
852 Westra, S. et al., 2014. Future changes to the intensity and frequency of short-duration extreme rainfall. Reviews of
853 Geophysics, 52(3): 2014RG000464. DOI:10.1002/2014RG000464
854 Westra, S., Sisson, S.A., 2011. Detection of non-stationarity in precipitation extremes using a max-stable process
855 model. Journal of Hydrology, 406(1-2): 119-128. DOI:DOI 10.1016/j.jhydrol.2011.06.014
856 Wood, E.F., Rodríguez-Iturbe, I., 1975a. A Bayesian approach to analyzing uncertainty among flood frequency models.
857 Water Resources Research, 11(6): 839-843. DOI:10.1029/WR011i006p00839
858 Wood, E.F., Rodríguez-Iturbe, I., 1975b. Bayesian inference and decision making for extreme hydrologic events. Water
859 Resources Research, 11(4): 533-542. DOI:10.1029/WR011i004p00533
860 Wu, A.M., Hsieh, W.W., Shabbar, A., 2005. The nonlinear patterns of North American winter temperature and
861 precipitation associated with ENSO. Journal of Climate, 18(11): 1736-1752. DOI:10.1175/jcli3372.1
862 Wu, R.G., Hu, Z.Z., Kirtman, B.P., 2003. Evolution of ENSO-related rainfall anomalies in East Asia. Journal of
863 Climate, 16(22): 3742-3758. DOI:Doi 10.1175/1520-0442(2003)016<3742:Eoerai>2.0.Co;2

864

865

# List of captions

## Tables

TABLE 1: SUMMARY OF GOODNESS-OF-FIT FOR ALL REGIONS. "#" MEANS "NUMBER OF".

TABLE 2: QUALITATIVE SUMMARY OF THE EFFECTS OF ENSO ON THE LOCATION AND SCALE PARAMETERS. ARROWS DENOTE AREAS WITH REMARKABLE EFFECT OF ENSO WHERE A SIGNIFICANT EFFECT IS FOUND IN MANY CONTINUOUS REGIONS WITHIN THE AREA. '↓' DENOTES A NEGATIVE EFFECT AND '↑' DENOTES A POSITIVE EFFECT ON THE LOCATION PARAMETER. SINGLE ARROW DESCRIBES A MODERATE EFFECT, WHILE DOUBLE ARROW DESCRIBES A STRONG EFFECT FOR THE ABSOLUTE SLOPE VALUE LARGER THAN 0.2. THE UNDERLINED ARROWS DESCRIBE THAT SAME EFFECT OF ENSO IS ALSO DETECTED ON THE SCALE PARAMETER.

TABLE 3: QUALITATIVE SUMMARY OF THE EFFECT OF ENSO ON QUANTILES. "↑" DENOTES THE SEASONS IN WHICH EL NIÑO/LA NIÑA HAS A POSITIVE EFFECT, WHILE "↓" DENOTES A NEGATIVE EFFECT. THE SEASONS ARE SORTED IN DESCENDING ORDER ACCORDING TO STRENGTH OF THE EFFECT OF ENSO. IF THE EFFECT THE ENSO IS NOT STRONG OVER THE WHOLE AREA, SUB-AREA WITH STRONG EFFECT IS SPECIFIED IN THE PARENTHESES.

## Figures

FIGURE 1: LOCATION OF HIGH QUALITY OBSERVATION SITES WITH MORE THAN 40 YEARS OF RECORD (RED DOTS) FROM HADEX2 DATASET. RESULTS OF THIS STUDY WILL BE SUMMARIZED FOR THE NINETEEN AREAS REPRESENTED BY BLACK BOXES.

FIGURE 2: SCHEMATIC OF OBSERVATION SITE SELECTION FOR EACH GRID CELL.

FIGURE 3: SLOPE OF THE LOCATION PARAMETER WITH RESPECT TO SOI DURING EL NIÑO ( $\mu_{reg_1}^{-}$ ) AND LA NIÑA ( $\mu_{reg_1}^{+}$ ) PHASES FOR DJF SEASON. SMALL GREY DOTS DENOTE CELLS WITH TOO FEW DATA STATIONS TO PERFORM A REGIONAL ANALYSIS. DOTS WITH RED (BLUE) OUTLINES DENOTE SIGNIFICANTLY POSITIVE (NEGATIVE) SLOPES, WHILE DOTS WITH GREY OUTLINES DENOTE NON-SIGNIFICANT SLOPES. DOTS WITH YELLOW OUTLINES DENOTE THE DRY REGIONS WITH FREQUENT ZERO PRECIPITATION DURING DJF.

FIGURE 4: SAME AS FIGURE 3, BUT FOR SCALE PARAMETERS $\sigma_{reg_1}^{-}$ (EL NIÑO) AND $\sigma_{reg_1}^{+}$ (LA NIÑA).

FIGURE 5: PERCENTAGE CHANGE FOR THE INTENSITY OF 1 IN 10 YEAR PRECIPITATION RELATIVE TO SOI=0 FOR INDIVIDUAL GAUGE LOCATIONS FOR DJF SEASON. GREY DOTS DENOTE CELLS WITH TOO LITTLE STATION DATA TO PERFORM A REGIONAL ANALYSIS. RED (BLUE) DOTS DENOTE AN INCREASE (DECREASE) IN THE INTENSITY OF A 1 IN 10 YEAR PRECIPITATION EVENT FOR STRONG EL NIÑO/LA NIÑA PHASES COMPARED WITH A NEUTRAL PHASE. YELLOW DOTS DENOTE THE DRY REGIONS WITH FREQUENT ZERO PRECIPITATIONS DURING DJF.

FIGURE 6: THE EFFECT OF EL NIÑO AND LA NIÑA ON THE 1 IN 10 YEAR PRECIPITATIONS FOR DIFFERENT SEASONS. SAMPLES FOR THE BOXPLOT ARE THE PERCENTAGE CHANGE MEDIAN OF THE PRECIPITATION CALCULATED AT EACH STATION WITHIN THE AREAS SHOWN IN FIGURE 1. THE SEASON WITH MODERATE OR STRONG EFFECT OF ENSO AS GIVEN BY TABLE 2 IS HIGHLIGHTED IN BOLD. (A HIGH RESOLUTION FIGURE IS AVAILABLE ONLINE).

FIGURE 7: CONCEPTUAL DIAGRAM OF THE TYPES OF SYMMETRY/ASYMMETRY IN THE RELATIONSHIP BETWEEN ENSO AND EXTREME PRECIPITATION. (A) SYMMETRIC RELATIONSHIP: OPPOSITE EFFECTS IN THE TWO PHASES; (B) ONE PHASE ASYMMETRIC RELATIONSHIP: NO EFFECT FOR ONE PHASE AND A STRONG EFFECT FOR THE OTHER PHASE; (C) TWO PHASE ASYMMETRIC RELATIONSHIP: STRONG, BUT NON-OPPOSITE ENSO EFFECT DURING BOTH THE EL NIÑO AND LA NIÑA PHASES.

## Supplement

S 1: (A) GOODNESS-OF-FIT PP-PLOT OF ALL SIXTEEN STATIONS. (B) DEPENDENCE-DISTANCE RELATIONSHIP OF THE GAUSSIAN TRANSFORMED DATA. THE BLACK DOTS ARE THE EMPIRICAL PAIRWISE CORRELATIONS AND RED LINES ARE THE ESTIMATION FROM THE EXPONENTIAL MODEL (EQ.(4)) WITH 90% CREDIBILITY INTERVAL.

S 2: POSTERIOR DISTRIBUTION OF THE REGIONAL PARAMETERS $\mu_{reg_1}^{-}$, $\mu_{reg_1}^{+}$ AND $\xi$. THE FIRST SIXTEEN BOXES ARE THE ESTIMATION WITH NON-INFORMATIVE PRIORS USING FROM ONE TO SIXTEEN STATIONS. THE LAST BOX IS THE ESTIMATION USING ALL SIXTEEN STATIONS WITH MARTINS AND STEDINGER' (MS) GAMMA(6,9) PRIOR FOR THE SHAPE PARAMETER.

S 3: SCATTERPLOT OF THE PROBABILITY OF A STATION PAIR EXCEEDING THE 75$^{TH}$ PERCENTILE OF THE AT-SITE HISTORICAL SEASONAL MAXIMUM DAILY PRECIPITATION AMONG THE STATIONS IN A REGION. (A) EMPIRICAL PROBABILITY VS. THEORETICAL PROBABILITY CALCULATED BY THE GAUSSIAN COPULA MODEL; (B) EMPIRICAL PROBABILITY VS. THEORETICAL PROBABILITY CALCULATED BY THE MODEL IGNORING SPATIAL DEPENDENCE. THE DASHED RED LINE IS THE FIT OF A CUBIC SMOOTHING SPLINE.

911

912 **Table 1: Summary of goodness-of-fit for all regions. "#" means "number of".**

| Season | # regions meeting data requirements | # regions with mostly zero values for seasonal maximum precipitation | # regions where goodness of fit is good | # regions where goodness of fit is poor |
|---|---|---|---|---|
| DJF | 323 | 12 | 309 | 2 |
| MAM | 323 | 13 | 309 | 1 |
| JJA | 323 | 21 | 301 | 1 |
| SON | 323 | 4 | 319 | 0 |

**Table 2: Qualitative summary of the effects of ENSO on the location and scale parameters. Arrows denote areas with remarkable effect of ENSO where a significant effect is found in many continuous regions within the area. '↓' denotes a negative effect and '↑' denotes a positive effect on the location parameter. Single arrow describes a moderate effect, while double arrow describes a strong effect for the absolute slope value larger than 0.2. The underlined arrows describe that same effect of ENSO is also detected on the scale parameter.**

| Group | Order | Area | ENSO effect on location and scale parameters | | | | | | | |
|---|---|---|---|---|---|---|---|---|---|---|
| | | | DJF | | MAM | | JJA | | SON | |
| | | | El Niño | La Niña | El Niño | La Niña | El Niño | La Niña | El Niño | La Niña |
| I | 1 | Western North America | ↓ | | ↑ | | | | ↑ | ↑ |
| | 2 | Central North America | ↑ | ↑ | | | | | ↑↑ | ↑↑ |
| | 3 | Eastern North America | | | | | | | | |
| | 4 | Southern North America | ↑↑ | ↓↓ | | ↓↓ | | | | |
| II | 5 | Northern Europe | ↑ | ↑ | | | | | | |
| | 6 | British Isles | | | | | | | | |
| | 7 | Central Europe | | | | | | | | |
| | 8 | Mediterranean | | | | | | | ↑↑ | |
| III | 9 | Northern Indian subcontinent | | ↓↓ | | ↑↑ | | | | ↑↑ |
| | 10 | Southern Indian subcontinent | | | | | | ↑↑ | | |
| | 11 | Northeast China | | | ↑ | | | | | |
| | 12 | Southeast China | ↑↑ | | | | | | | |
| | 13 | Northern Southeast Asia | ↓↓ | ↑↑ | | ↑↑ | | ↓↓ | ↓↓ | ↑↑ |
| IV | 14 | Southeast South America | ↑↑ | | ↑↑ | | | | | ↓↓ |
| | 15 | South Africa | ↓ | ↑↑ | | ↑↑ | | | | |
| | 16 | Southwest Western Australia | | ↑↑ | | ↑↑ | | | | |
| | 17 | Southern Australia | | | | ↑↑ | ↓ | ↑ | ↓↓ | |
| | 18 | Eastern Australia | | ↑↑ | | | ↓↓ | | ↓↓ | ↑↑ |
| | 19 | New Zealand | | | | | | | | |

**Table 3: Qualitative summary of the effect of ENSO on quantiles. "↑" denotes the seasons in which El Niño/La Niña has a positive effect, while "↓" denotes a negative effect. The seasons are sorted in descending order according to strength of the effect of ENSO. If the effect the ENSO is not strong over the whole area, sub-area with strong effect is specified in the parentheses.**

| | Group | Area | El Niño | La Niña | Asymmetry |
|---|---|---|---|---|---|
| Most affected regions | I | Central North America | ↑SON,DJF | ↑SON,DJF | Asymmetric, 2 phases |
| | | Southern North America | ↑DJF | ↓MAM,DJF (southern US) | Symmetric |
| | III | Northeast China | ↑DJF,MAM | ↑DJF,MAM | Asymmetric, 2 phases |
| | | Southeast China | ↑DJF | / | Asymmetric, 1 phase |
| | | Northern Southeast Asia | ↓DJF,SON | ↑DJF,MAM,SON, ↓ JJA | Symmetric |
| | IV | Southeast South America | ↑DJF,MAM | ↓SON | Asymmetric, 1 phase |
| | | South Africa | / | ↑DJF,MAM | Asymmetric, 1 phase |
| | | Southwest Western Australia | / | ↑DJF,MAM | Asymmetric, 1 phase |
| | | Southern Australia | ↓SON,JJA | ↑MAM,JJA,SON | Asymmetric, 1 phase (MAM); Symmetric (SON,JJA) |
| | | Eastern Australia | ↓JJA, SON | ↑DJF,SON | Asymmetric, 1 phase (DJF, JJA); Symmetric (SON) |
| Other affected regions | I | Western North America | ↑SON,MAM ↓ DJF | ↑SON | Asymmetric, 2 phases |
| | II | Northern Europe | ↑DJF | ↑DJF | Asymmetric, 2 phases |
| | | Mediterranean | ↑SON (eastern part) | / | Asymmetric, 1 phase |
| | III | Northern Indian subcontinent | / | ↑SON,MAM, ↓ DJF | Asymmetric, 1 phase |
| | | Southern Indian subcontinent | / | ↑JJA | Asymmetric, 1 phase |

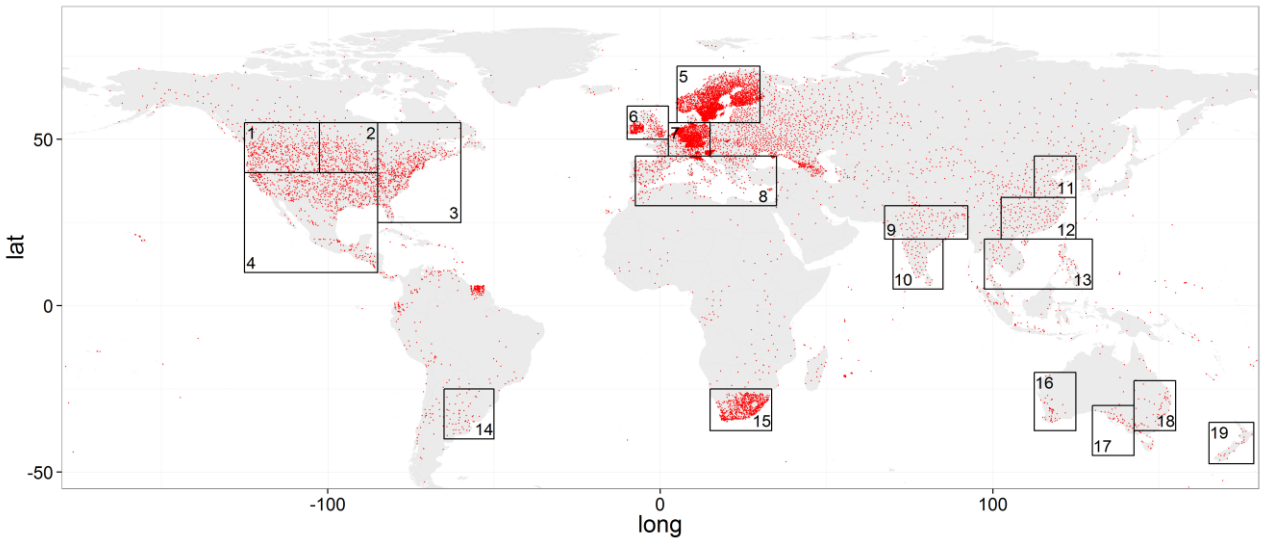


913 **Figure 1: Location of high quality observation sites with more than 40 years of record (red**
914 **dots) from HadEX2 dataset. Results of this study will be summarized for the nineteen areas**
915 **represented by black boxes.**

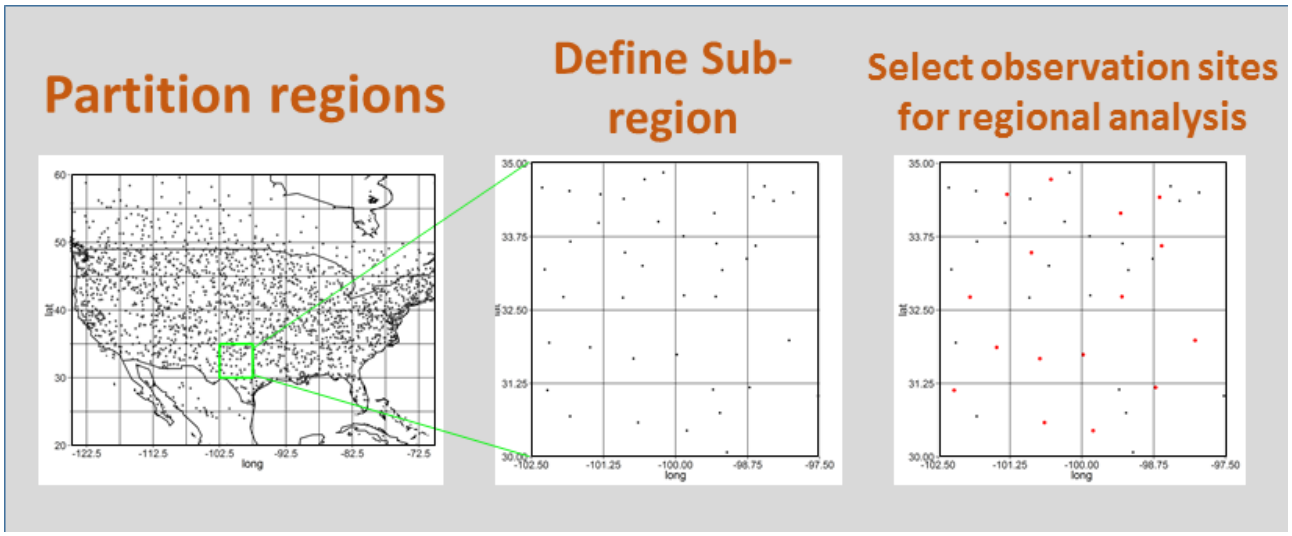


916 **Figure 2: Schematic of observation site selection for each grid cell.**

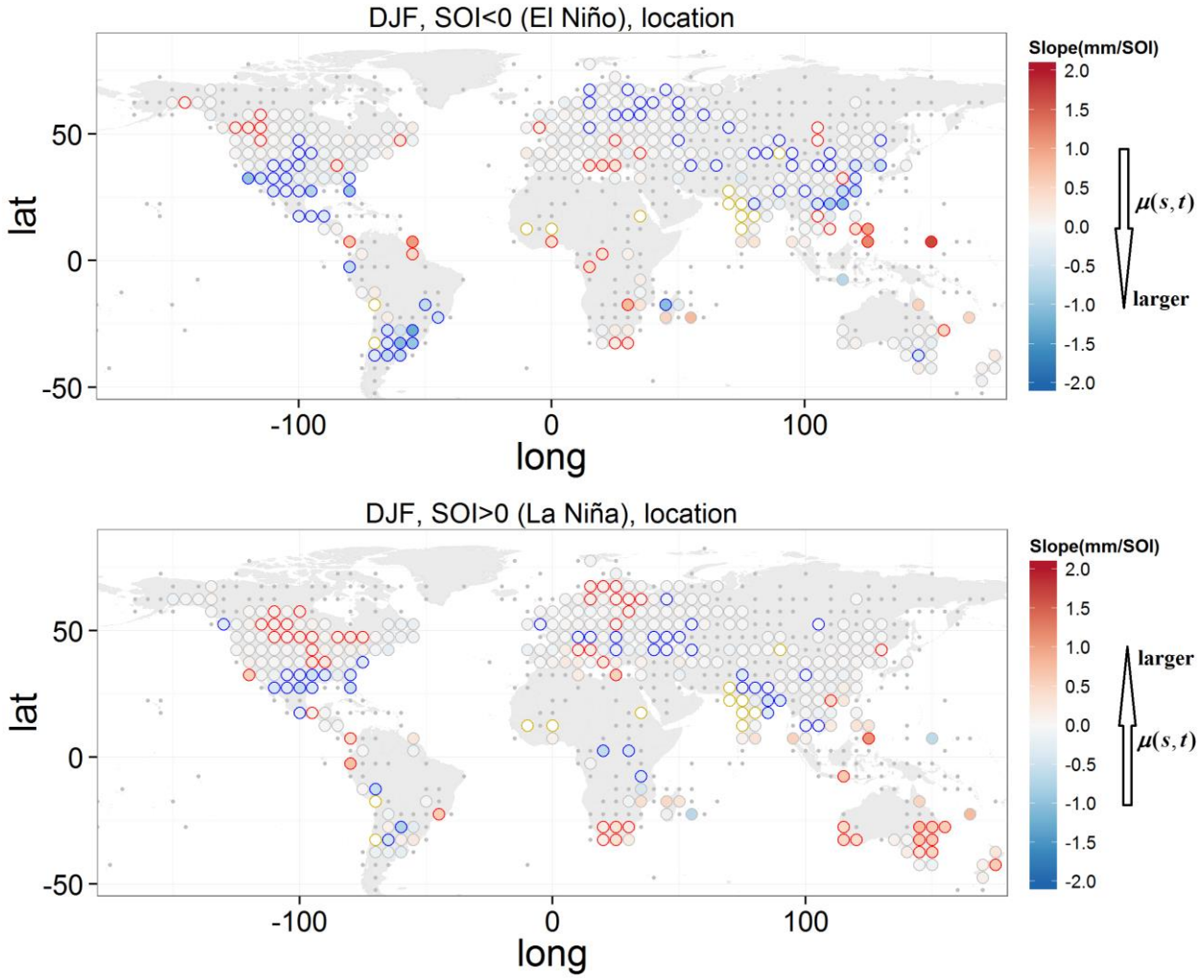


**Figure 3: Slope of the location parameter with respect to SOI during El Niño ($\mu^{-}_{reg_1}$) and La Niña ($\mu^{+}_{reg_1}$) phases for DJF season. Small grey dots denote cells with too few data stations to perform a regional analysis. Dots with red (blue) outlines denote significantly positive (negative) slopes, while dots with grey outlines denote non-significant slopes. Dots with yellow outlines denote the dry regions with frequent zero precipitation during DJF.**

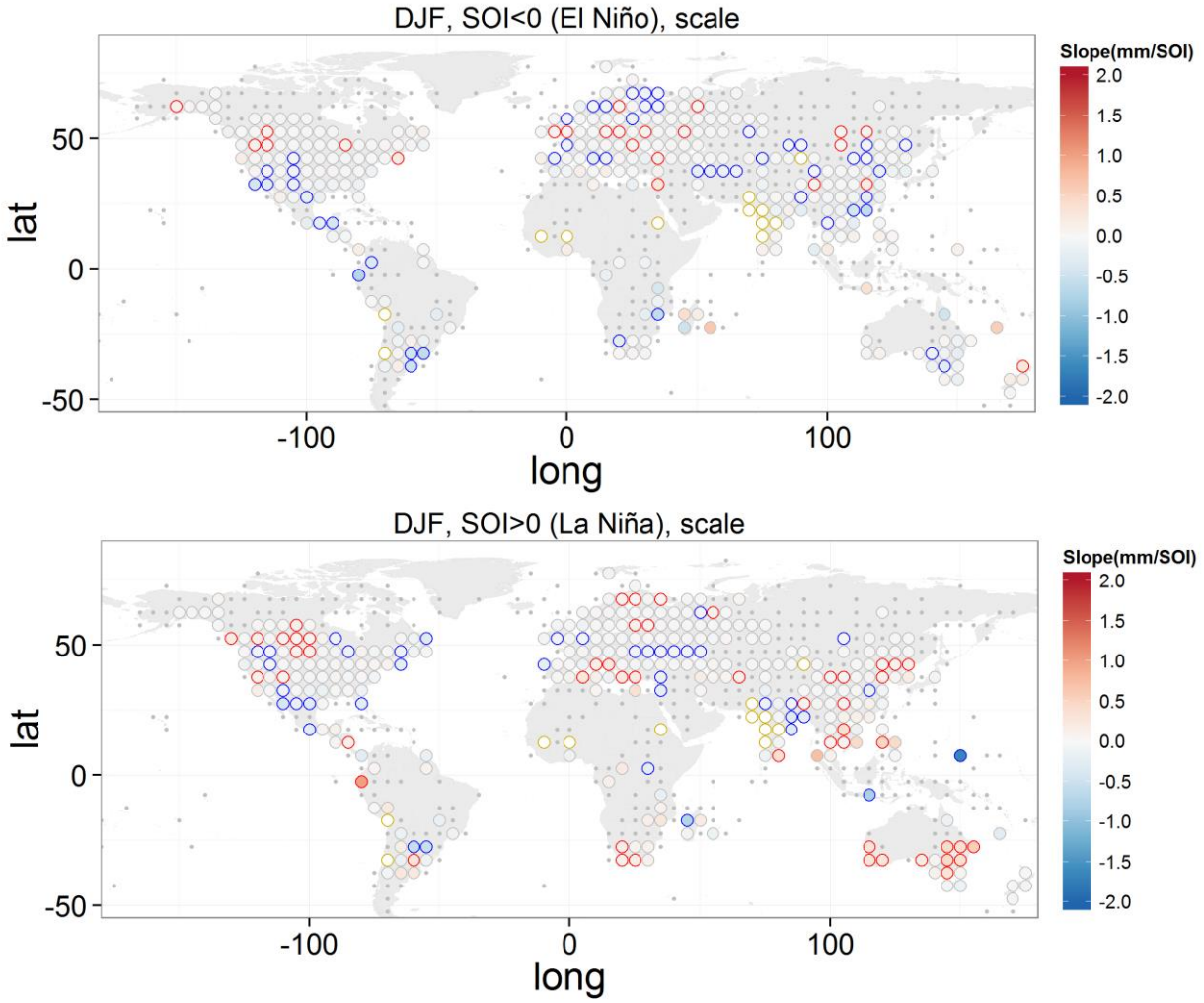


922 **Figure 4: Same as Figure 3, but for scale parameters $\sigma^{-}_{reg_1}$ (El Niño) and $\sigma^{+}_{reg_1}$ (La Niña).**

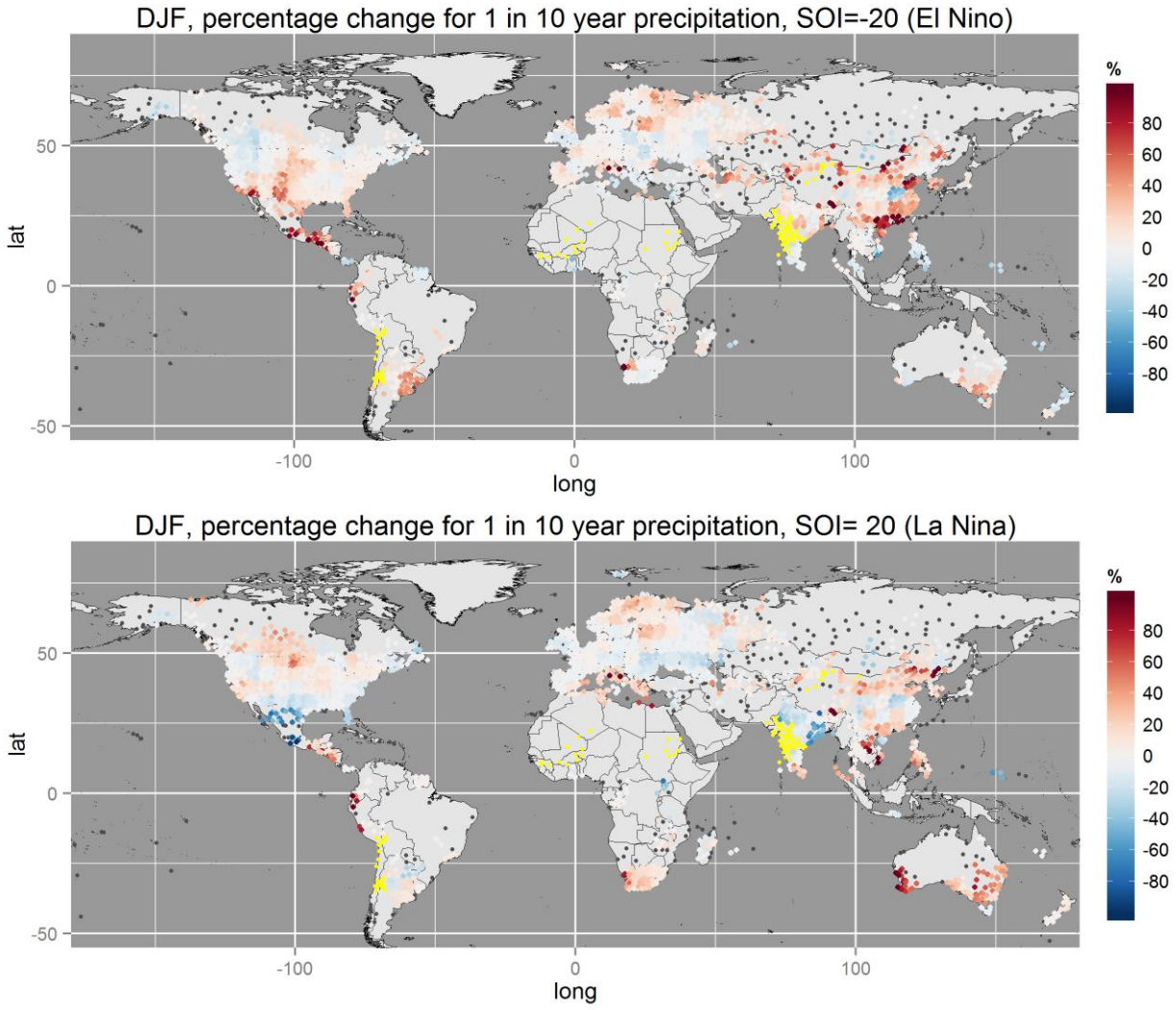


**Figure 5: Percentage change for the intensity of 1 in 10 year precipitation relative to SOI=0 for individual gauge locations for DJF season. Grey dots denote cells with too little station data to perform a regional analysis. Red (blue) dots denote an increase (decrease) in the intensity of a 1 in 10 year precipitation event for strong El Niño/La Niña phases compared with a neutral phase. Yellow dots denote the dry regions with frequent zero precipitations during DJF.**

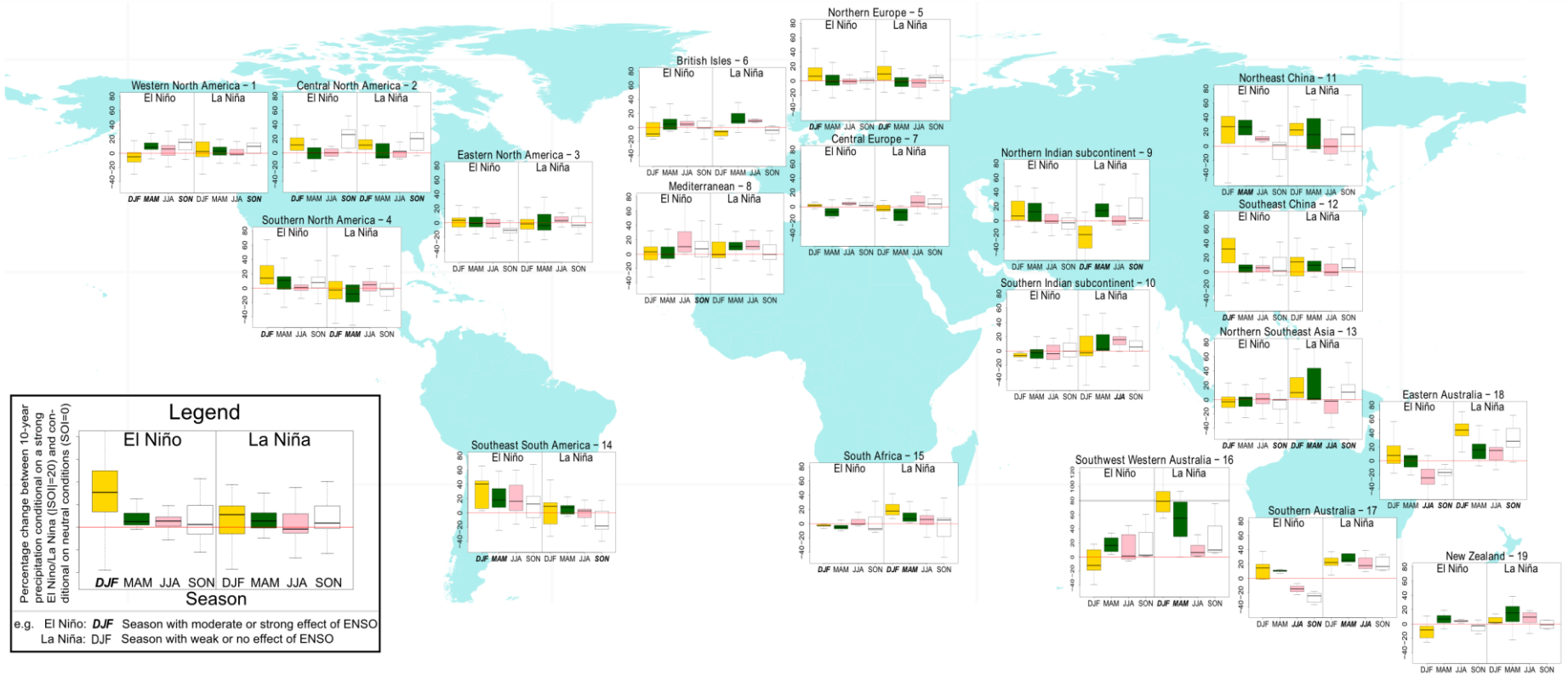


929 **Figure 6: The effect of El Niño and La Niña on the 1 in 10 year precipitations for different seasons. Samples for the boxplot are the**
930 **percentage change median of the precipitation calculated at each station within the areas shown in Figure 1. The season with moderate**
931 **or strong effect of ENSO as given by Table 2 is highlighted in bold. (A high resolution figure is available online).**

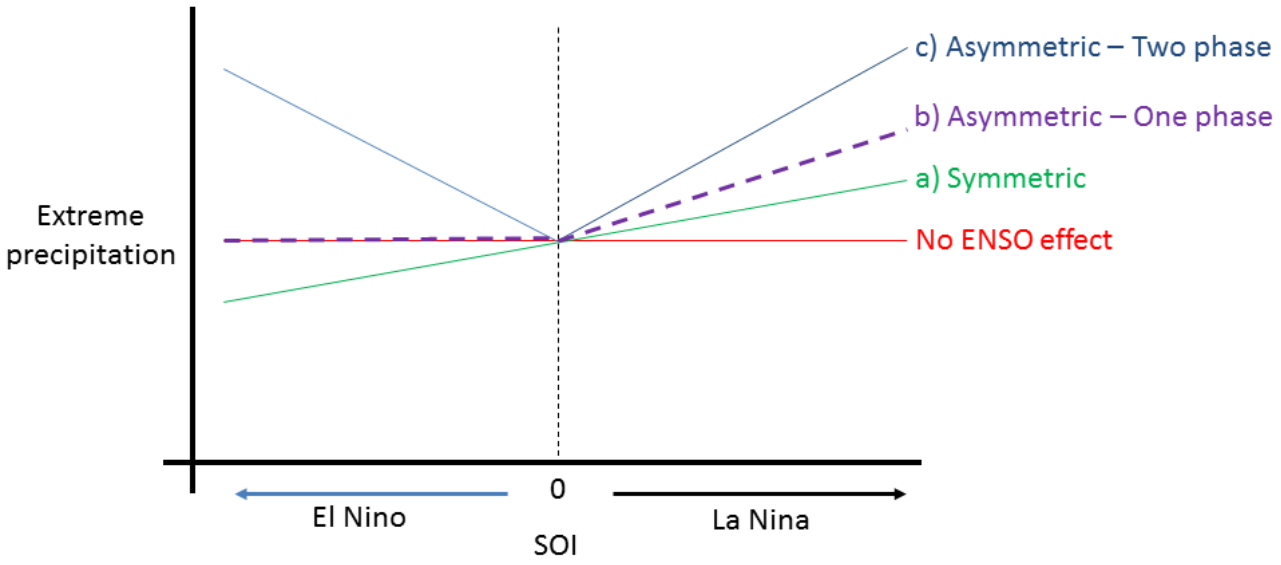


**Figure 7: Conceptual diagram of the types of symmetry/asymmetry in the relationship between ENSO and extreme precipitation. (a) Symmetric relationship: opposite effects in the two phases; (b) One phase asymmetric relationship: no effect for one phase and a strong effect for the other phase; (c) Two phase asymmetric relationship: strong, but non-opposite ENSO effect during both the El Niño and La Niña phases.**

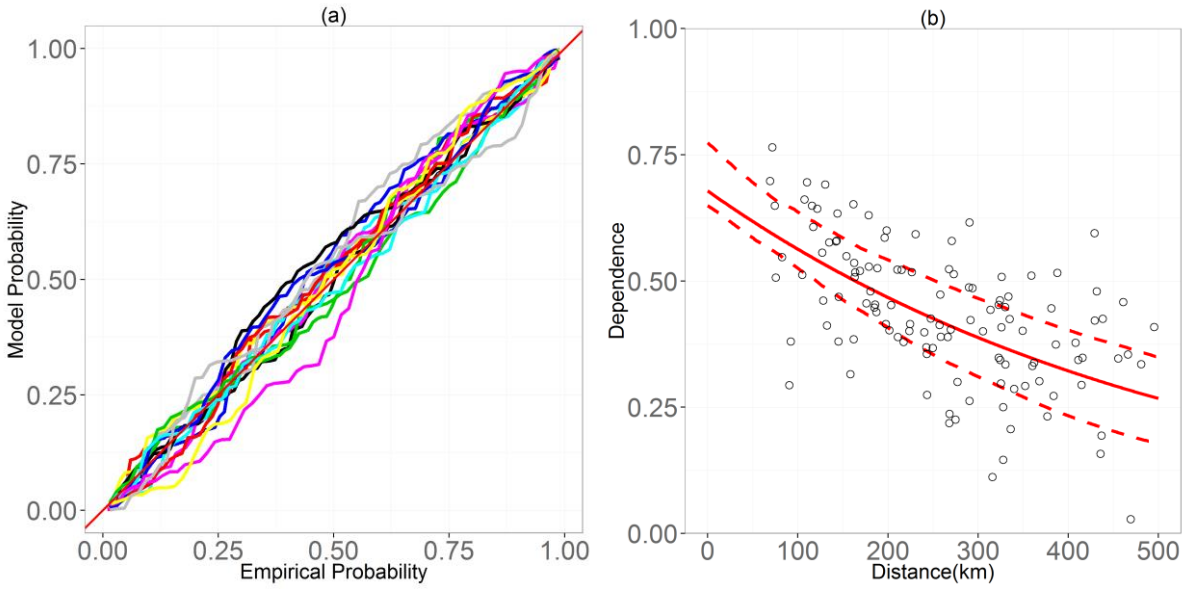


**S 1: (a) Goodness-of-fit PP-plot of all sixteen stations. (b) Dependence-distance relationship of the Gaussian transformed data. The black dots are the empirical pairwise correlations and red lines are the estimation from the exponential model (Eq.(4)) with 90% credibility interval.**

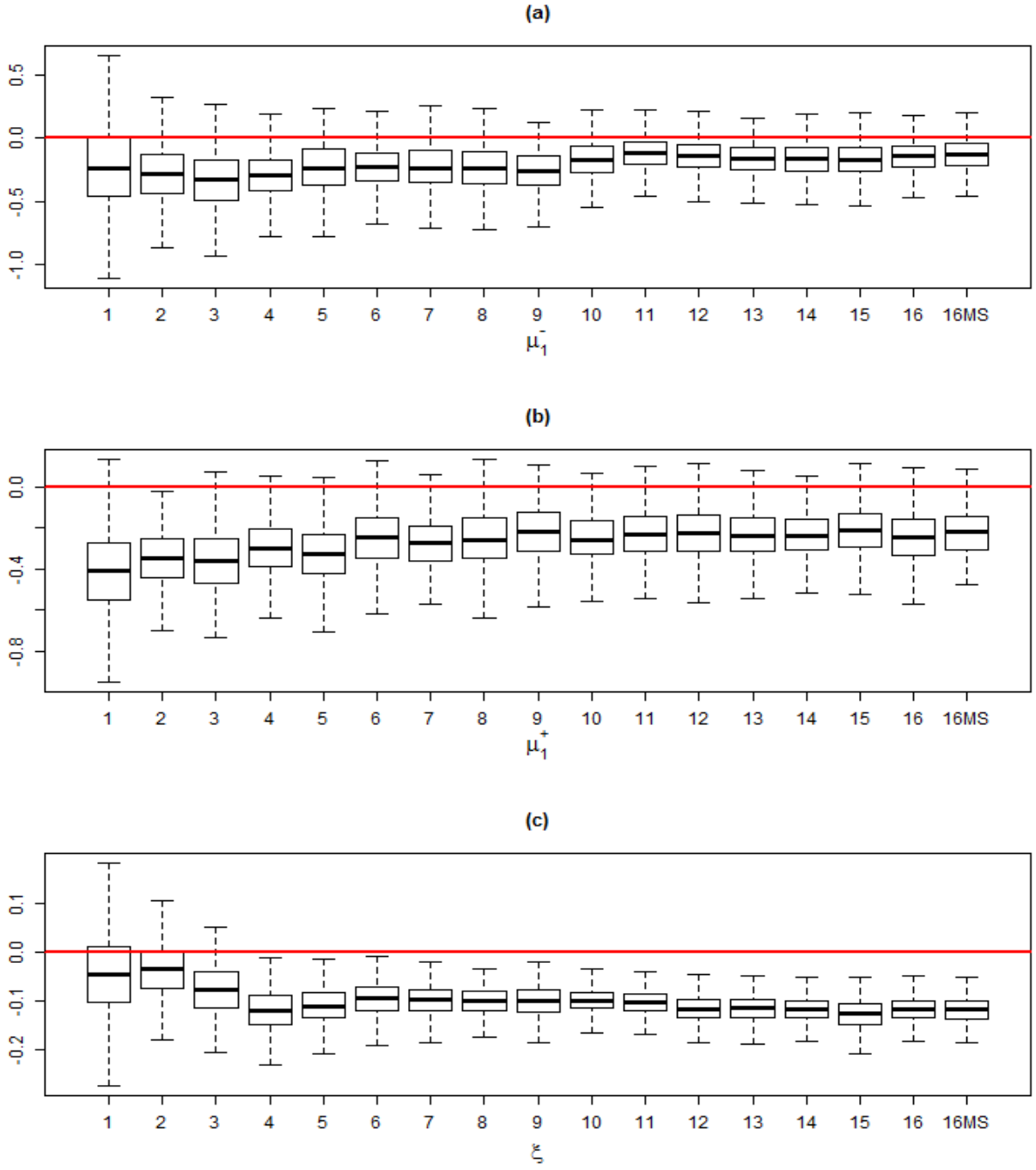


940 **S 2: posterior distribution of the regional parameters $\mu_{reg_1}^-$, $\mu_{reg_1}^+$ and $\xi$. The first sixteen boxes**
941 **are the estimation with non-informative priors using from one to sixteen stations. The last box**
942 **is the estimation using all sixteen stations with Martins and Stedinger' (MS) Gamma(6,9)**
943 **prior for the shape parameter.**

944

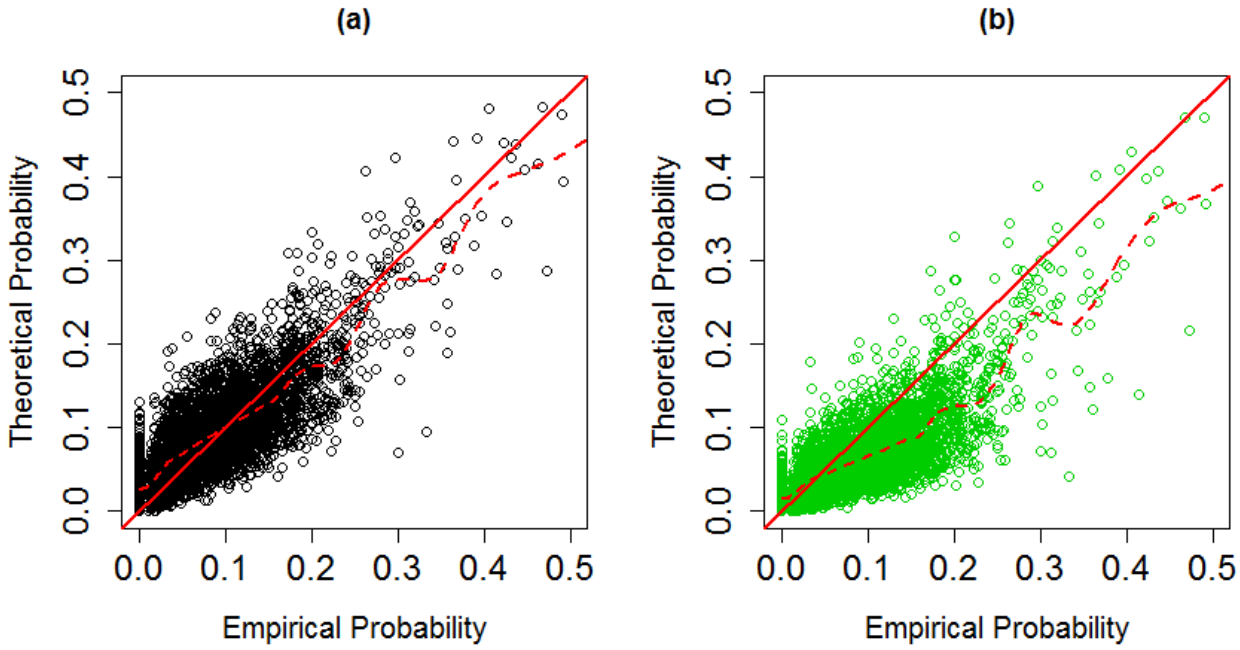


945

946 **S 3: Scatterplot of the probability of a station pair exceeding the 75$^{th}$ percentile of the at-site**
947 **historical seasonal maximum daily precipitation among the stations in a region. (a) Empirical**
948 **probability vs. Theoretical probability calculated by the Gaussian copula model; (b)**
949 **Empirical probability vs. Theoretical probability calculated by the model ignoring spatial**
950 **dependence. The dashed red line is the fit of a cubic smoothing spline.**